A spectral boundary-integral method for faults and fractures in a poroelastic solid: Simulations of a rate-and-state fault with dilatancy, compaction, and fluid injection

Elías Rafn Heimisson[1,2], Shengduo Liu[3], Nadia Lapusta[2,3], John Rudnicki[4]

[1]Swiss Seismological Service, ETH Zurich, Zurich, Switzerland
[2]Division of Geological and Planetary Sciences, California Institute of Technology, Pasadena, CA, USA
[3]Division of Engineering and Applied Science, California Institute of Technology, Pasadena, California, USA
[4]Department of Civil and Environmental Engineering and Department of Mechanical Engineering, Northwestern University, Evanston, IL, USA

Key Points:

- We present a novel spectral boundary-integral method (SBIM) for a 2D poroelastic solid
- We solve for fault slip with fully-coupled dilatancy and injection on a rate-and-state fault
- The method is applied to study the influence of several parameters on fault stability

Corresponding author: Elías Rafn Heimisson, elias.heimisson@sed.ethz.ch

Abstract

Fluid-fault interactions result in many two-way coupled processes across a range of length scales, from the micron scale of the shear zone to the kilometer scale of the slip patch. The scale separation and complex coupling render fluid-fault interactions challenging to simulate and may ultimately limit our understanding of experimental data and induced seismicity. Here we present spectral boundary-integral solutions for in-plane interface sliding and opening in a poroelastic solid. We solve for fault slip in the presence of rate-and-state frictional properties, inelastic dilatancy, injection, and the coupling of a shear zone and a diffusive poroelastic bulk. The shear localization zone is treated as having a finite-width and non-constant pore pressure, albeit with a simplified mathematical representation. The dimension of the 2D plane strain problem is reduced to a 1D problem resulting in increased computational efficiency and incorporation of small-scale shear-zone physics into the boundary conditions. We apply the method to data from a fault injection experiment that has been previously studied with modeling. We explore the influence of inelastic dilatancy, bulk poroelastic response, and bulk diffusivity on the simulated fault slip due to the injection. Dilatancy not only alters drastically the stability of fault slip but also the nature of pore pressure evolution on the fault, causing significant deviation from the standard square-root-of-time diffusion. More surprisingly, varying the bulk's poroelastic response (by using different values of the undrained Poisson's ratio) and bulk hydraulic diffusivity can be as critical in determining rupture stability as the inelastic dilatancy.

Plain Language Summary

Earthquakes occur on faults deep in the Earth's crust. At this depth, the faults are surrounded by rock and water that fills up pores and fractures in the rock. This water affects how the surrounding crust responds to earthquakes or slip on the faults. Water also plays an important role within the faults since it will decrease or increase the frictional resistance if it causes pressurization or depressurization, respectively. A common cause of pressurization in faults is by an injection of fluid, which is done for many different purposes ranging from geothermal exploitation, carbon sequestration, or wastewater disposal. Here we develop a new efficient method to simulate fault slip and earthquakes in a porous and fluid-filled medium. This allows us to better understand the role of water in earthquake processes, either in the medium surrounding the fault or within

the fault. We compare our method to a previously studied experiment where water was injected directly into a fault and slip measured. In addition, we investigate certain physical properties of the porous rock that have not received much attention in the literature. We find that they significantly influence if earthquakes occur due to injection.

1 Introduction

The role of fluids in seismic and aseismic faulting processes has been of significant interest in the last few years. Mounting evidence indicates that fluids may play an important role in a diverse set of mechanisms that alter fault slip behavior ranging from earthquake triggering to slow slip events.

The most prominent example of fluid and fault interactions is the clear link between fluid injection and induced seismicity, as originally pointed out by Raleigh et al. (1976); Hsieh and Bredehoeft (1981) and remains a critical issue (e.g. Ellsworth, 2013). This phenomenon has a straightforward mechanical explanation: higher pore pressures, due to injection, reduce the effective normal stress and thus the frictional resistance of the fault. The fault then slips faster and may accelerate the generation of seismic instabilities. This problem has been frequently modeled with a straightforward implementation of one-way coupling of pore pressure and frictional strength where pore pressure perturbations are imposed and slip or number of seismic events are computed. Injection into faults may lead to sustained aseismic transients (e.g. Viesca & Dublanchet, 2019; Bhattacharya & Viesca, 2019), which may later become seismic events depending on the frictional properties of the fault (Larochelle et al., 2021a). A more detailed investigation of this problem reveals considerable complexity in pore pressure evolution if heterogeneous permeability structures and poroelasticity are considered (e.g. Yehya et al., 2018)

The poroelastic properties of the crust have lately been receiving more interest, most prominently as a long-ranging and fast-acting mechanism in which faults can be stressed due to injection or extraction (Segall & Lu, 2015). However, there is also significant literature on the role of poroelasticity in influencing the nucleation or propagation of seismic and aseismic ruptures (Rudnicki & Koutsibelas, 1991; Dunham & Rice, 2008; Jha & Juanes, 2014; Heimisson et al., 2019, 2021). An effect of particular importance in regard to the influence of poroelasticity is that, during in-plane sliding, compression and dilation of the host rock induces pore pressure change in the shear zone (Heimisson et

al., 2019, 2021); this effect is discussed further in section 1.1. Thus the poroelastic response of the bulk, induced by an ongoing rupture, may influence the effective normal stress and hence shear resistance to the rupture, creating a feedback loop. Poroelasticity also influences and introduces a diffusion-dependent time-evolving shear stress on the fault plane with significant implications for the stability of sliding (Heimisson et al., 2021).

Processes other than poroelasticity may change pore pressure in an active shear zone and affect rupture and instability formation on faults. The generation of aseismic slip transients on faults is believed to be related to pore fluids. For example, transient slow slip events (SSEs) in subduction zones are thought to be related to high pore pressure conditions (e.g., Liu & Rice, 2007; Bürgmann, 2018). A primary challenge in explaining the mechanics of transient slow slip is to understand why it starts, but does not become an earthquake. One potential mechanism is a geometric restriction, in which the high-pore-pressure region is large enough to cause slip acceleration, for example, due to rate-and-state velocity-weakening friction properties, but too small for that slip to become seismic (Liu & Rice, 2005, 2007). Another potential explanation is the change from velocity-weakening to velocity-strengthening friction with increasing slip rates (Shibazaki & Shimamoto, 2007; Hawthorne & Rubin, 2013; Leeman et al., 2016). Rate-and-state faults with velocity-strengthening friction and additional destabilizing effects can also produce SSEs in models with poroelasticity (Heimisson et al., 2019) and viscoplasticity (Tong & Lavier, 2018). Inelastic dilatancy of granular fault gouge, which can lead to a reduction in pore pressure and stabilize fault slip, has been highlighted as a naturally present fluid-related mechanism that can explain how slow slip transients do not evolve into seismic events (e.g. Segall & Rice, 1995; Segall et al., 2010). Modeling of fault slip with inelastic dilatancy can explain many properties of slow slip events, including their scaling (Dal Zilio et al., 2020).

Multiple mechanisms may act at a time. Recently, numerical simulations have started exploring the simultaneous injection and inelastic dilatancy in a diffusive shear zone (Ciardo & Lecampion, 2019; Yang & Dunham, 2021). However, these efforts have been limited to a non-diffusive and elastic bulk. Coupling with a poroelastic bulk introduces another degree of complexity, where elastic dilation and compression of the bulk generate pore pressure transients. Further complexity is introduced by field observations indicating that permeability of the shear zone in a fault core may be very different from the surrounding damage zone and host rock (e.g. Wibberley & Shimamoto, 2003). Further, the shear-

ing of gouge material can dramatically reduce the permeability perpendicular to the shearing direction and thus result in the shear zone having a significantly anisotropic permeability (Zhang et al., 1999).

Here we present a spectral boundary-integral method that allows us to simulate quasi-dynamic slow and fast slip on a rate-and-state fault with dilatancy/compaction and fluid flow in a plane-strain poroelastic medium. We take a boundary layer approach where the outer solution, which is the spectral representation of the poroelastic bulk, treats the fault as a zero-thickness interface with suitable boundary conditions. However, the inner solution considers the fault to be a finite-width shear zone. We consider the frictional properties of the shear zone to be determined by its width-averaged properties. The bulk is an isotropic standard quasi-static Biot poroelastic solid with a hydraulic diffusivity c. The shear zone has frictional strength described by rate-and-state friction, with inelastic state-dependent dilatancy and compaction and anisotropic permeability: the permeability across the shear zone is different than the permeability along the shear zone. The inelastic state-dependent dilatancy and compaction are implemented using the Segall and Rice (1995) approach, as explained later. We frequently refer to this process only as "dilatancy" for the sake of brevity, and that is also how it is commonly referred to in the fault mechanics community. However, we remind the reader that the "dilatancy" law also predicts compaction under certain conditions. The pore pressure in the layer is simplified and assumed to be bi-linear where the two linear profiles are continuous at the center of the shear zone (as in Heimisson et al., 2021, see also section 1.1). The spectral representation uses analytical convolution kernels, which are truncated for efficiency similar to Lapusta et al. (2000), but at time scales relevant for the bulk diffusion at the specific wavenumber.

When slip speed becomes high enough in a narrow enough shear layer with small enough permeability, then thermal pressurization of pore fluids due to shear heating may also become important (e.g. Rice, 2006; Bizzarri & Cocco, 2006). While such effects may be critical for seismic rupture evolution (e.g. Noda & Lapusta, 2013), they may be negligible or at least much less pronounced in the nucleation phases of the seismic cycle (Segall & Rice, 2006; Segall, 2010), which are primarily the focus of this study. Consequently, we do not account for thermal pressurization.

The paper first discusses the general problem setup (section 1.1). For completeness, there is a quick review of governing equations and boundary conditions (section 2). However, we highlight that a more complete description is found in Heimisson et al. (2021) with the exception of added complexity introduced into the fluid mass balance (section 2.3.1) not included in previous work. In section 3, we provide the analytical spectral boundary-integral solutions for sliding and opening of an interface in a plane-strain poroelastic solid. The numerical approach taken to solve the coupled problem - with dilatancy, compaction, and injection in a poroelastic solid - is described in section 4. Finally, we show an application of the method (section 5), where we use constraints from a field experiment (Guglielmi et al., 2015) and a recent numerical study that modeled the field experiment data (Larochelle et al., 2021a). Finally, we discuss the role of poroelasticity, and other fluid-based mechanisms, in the dynamics of injection-induced seismic and aseismic slip.

1.1 Problem description

The general problem setup can be divided into three domains. Two are isotropic poroelastic half-spaces, which we call the bulk, one in $y > 0$ region and the other in $y < 0$ region. The third is a shear zone made from fault gouge, which separates the two half-spaces (Figure 1a). The two poroelastic half-spaces are assumed to have the same material properties, which we characterize through the shear modulus G, Skempton's coefficient B, drained Poisson's ratio ν, undrained Poisson's ratio ν_u, and hydraulic diffusivity c (e.g., Cheng, 2016; Detournay & Cheng, 1995; Rice & Cleary, 1976). In some cases, other poroelastic parameters may be displayed for compactness, legibility, and intuition. However, the implementation of the method we present uses the aforementioned five.

The shear zone is a thin layer of half-width ϵ. Here thin indicates that ϵ should be much smaller than any significant variation in fields, such as slip or pressure, along the $x-axis$, which is fundamental for accuracy of the boundary-layer treatment of the shear zone. The properties of the shear zone or fault gouge are characterized by reference porosity ϕ_0, inelastic dilatancy coefficient γ (Segall & Rice, 1995), and pore-pressure and normal-stress dependent void-volume compressibilities β_n^p and β_n^σ. In addition, the intact gouge material compressibilities are β_g^p and β_g^σ, and the fluid compressibilities are β_f^p and β_f^σ. The frictional strength of the shear zone is determined by the reference coefficient of fric-

tion f_0, the characteristic state evolution distance L, the constitutive parameter a that scales the direct rate dependence of friction, and the constitutive parameter b that scales the state dependence of friction. These parameters and properties of the shear zone are the same as in Heimisson et al. (2021) where a more detailed discussion is offered. We also note that their meaning is presented in the context of the governing equations in section 2. The hydraulic properties of the layer are somewhat different here compared to Heimisson et al. (2021). First, we consider that there may be a source of fluid mass in the layer, for example by injection, indicated by Q. Second, we include an anisotropic mobility (permeability over dynamic fluid viscosity). In particular, the mobility in the y direction, κ_{cx} can be different from the mobility in the x direction κ_{cy}. Thus, fluids injected into the fault have multiple migration paths, along the shear zone, perpendicular to the shear zone, and in both x and y directions in the bulk. Furthermore, an increase in pore pressure in the bulk can migrate into the shear zone and also into the bulk on the other side. (Figure 1a)

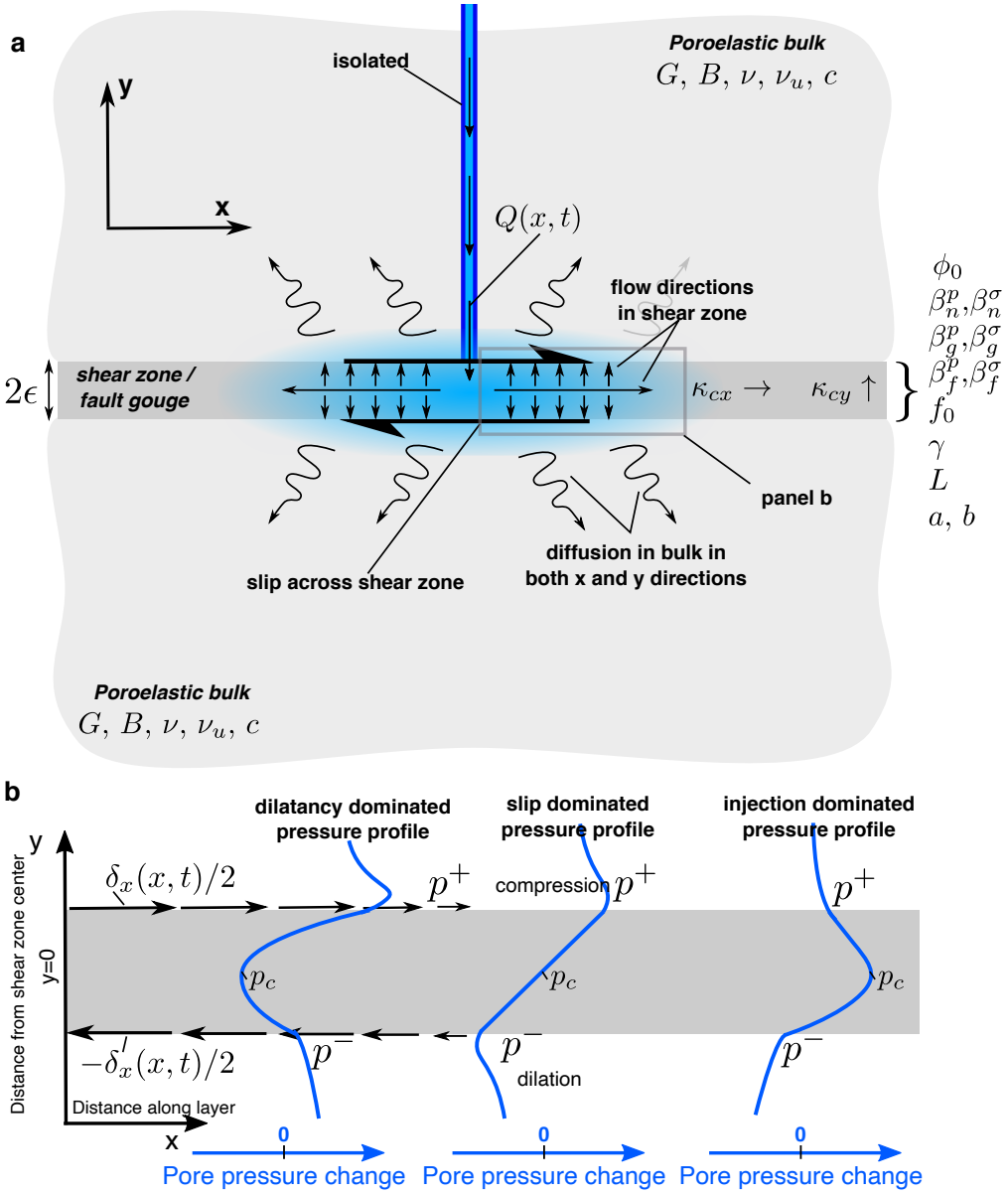

Figure 1. Schematic overview of the problems setup and possible pore pressure profiles scenarios in the shear zone. **a** Injection occurs in a thin shear zone embedded between two poroelastic solids of the same properties. This injection causes fluid migration along the shear zone, across the shear zone, and into the bulk. The evolving pore fluid pressure leads to slip across the shear zone. **b** Pore pressure profiles that can occur during the propagation of a single rupture induced by injection. If the pore pressure diffusion is ahead of the rupture, then the shear zone has increased pressure at the center p_c (right-most profile). Once considerable slip has occurred the inelastic dilatancy may have reduced the pressure, even to the point of being less than hydrostatic, which we may call a dilatancy dominated pore pressure (left-most profile). Between the two cases of an injection dominated regime and a dilatancy dominated regime we expect at or near the rupture tip the two effects may cancel. However, the compression and dilation of the host rock induced by the inhomogeneous slip can significantly change the pore pressures on either side of the shear zone (p^+ and p^-).

A key question in induced seismicity is to understand when so-called runaway ruptures happen, that is ruptures that propagate well outside a pressurized region. This is a useful focal point to explain some of the general dynamics that we expect from the described problem above. When injection into a fault occurs, there are two important length scales along the x dimension (Figure 1) that can interact and explain the dynamics of the slip. First, how far the pressure front from the injection site has diffused, which we can define as the region of significantly elevated pore pressure. Second, how far the rupture tip has propagated, which can be understood as the region of significant fault slip. If a fault has relatively low shear stress, i.e., its shear stress over initial effective normal stress is significantly below its reference friction coefficient, or is well-healed, which may be common in injection experiments, the pore pressure front controls how far the rupture tip can move since the frictional resistance is too great outside the pressure front (e.g., Larochelle et al., 2021a). However, if a fault is relatively well-stressed, or if the slipping region enters a more well-stressed portion of the fault or a portion of the fault with lower friction, then the rupture may become self-sustained and rupture outside the pressure front. Thus the rupture may initially be contained by the pressure front, but evolve to become a runaway rupture.

The interplay of the rupture tip and pressure front provides a useful qualitative explanation of the transition from a confined to runaway rupture. However, additional complexity, which is related to the pressure profile across the fault, plays an important role in determining the if, when or how such a rupture can happen. If a rupture is initiated in a shear zone by injection, the pressure profile across the shear zone (i.e. pressure change with y, Figure 1**b**) can be dominated by different mechanisms depending on whether observing the profile at a x coordinate that is ahead of the rupture, at the tip or behind the tip (Figure 1b). This will be particularly prominent for an in-plane rupture direction due to the volumetric straining of the bulk. If the pressurized zone is ahead of the rupture the shear zone central pressure (p_c) will be elevated. The pore pressures adjacent to the shear zone (p^+ and p^-) will also be elevated due to the leak-off into the bulk. Near the tip region, the influence of dilatancy has started to lower the pore pressure p_c, but furthermore volumetric straining of the bulk has caused an increase in pore pressure on the compressive side (p^+) and decrease on the dilating side (p^-) due to poroelastic coupling. Finally, behind the tip dilatancy may have further reduced the pressure p_c and possibly reversed the sign compared to the background equilibrium pressure and caused

flow back into the shear zone. We thus suggest that in order to model rupture propagation, earthquake nucleation, and understand runaway ruptures in a fluid-saturated medium due to injection, we must consider coupling that arises from the interplay of several mechanisms that alter the pore pressure.

2 Governing equations

This section will describe the conservation laws, friction laws, and boundary conditions. All the governing equations and boundary conditions with the exception of Section 2.3.1, which describes the fluid mass balance, are the same as in Heimisson et al. (2021). We state the equation with brief explanations for completeness, but refer the reader to Heimisson et al. (2021) for more elaborate discussion and derivations.

2.1 Poroelastic Bulk

The quasi-static theory of poroelasticity can be described as four coupled partial differential equations written in terms of displacements u_i and pressure changes p relative to an equilibrium pressure state (e.g., Detournay & Cheng, 1995; Cheng, 2016)

$$G u_{i,kk} + \frac{G}{1-2\nu} u_{k,ki} = \alpha p_{,i} \tag{1}$$

and

$$\frac{1}{M} p_{,t} - \kappa p_{,kk} = -\alpha u_{k,kt}, \tag{2}$$

where the material parameters are as follows: G: shear modulus, ν: drained Poisson's ratio, α: Biot-Willis parameter, M: Biot modulus, and κ is the mobility (the ratio between the permeability and fluid viscosity). In later expressions a different set of poroelastic material parameter may be used for compactness and increased intuition.

In this work, we assume plane strain deformation, in which case the governing equations can be reduced to three. Further simplification and decoupling of the governing equations is possible by using the McNamee-Gibson displacement functions (McNamee & Gibson, 1960; Verruijt, 1971). In obtaining solutions to equations (1) and (2) we follow the strategy explained in the Appendix of Heimisson et al. (2019) using the McNamee-Gibson displacement functions but using the boundary conditions listed in the next section.

2.1.1 Boundary conditions

Here we apply the same boundary conditions as in (Heimisson et al., 2021) at the interface, i.e. the shear zone and at infinity.

$$\lim_{y\to 0^{\pm}} u_x^{+} - u_x^{-} = \delta_x, \tag{3}$$

$$\lim_{y\to 0^{\pm}} u_y^{+} - u_y^{-} = \delta_y, \tag{4}$$

$$\lim_{y\to \pm\infty} u_x^{\pm} = 0 \text{ and } u_y^{\pm} = 0, \tag{5}$$

$$\lim_{y\to \pm\infty} p^{\pm} = 0, \tag{6}$$

$$\lim_{y\to 0^{\pm}} \sigma_{xy}^{+} - \sigma_{xy}^{-} = 0, \tag{7}$$

$$\lim_{y\to 0^{\pm}} \sigma_{yy}^{+} - \sigma_{yy}^{-} = 0, \tag{8}$$

where we have dropped the index notation and used x and y (as represented in Figure 1a).

The pore pressure in the shear zone is assumed to be bi-linear as in Heimisson et al. (2021) This is a generalization of the leaky interface used in the plane strain dislocation solution of Song and Rudnicki (2017). The pore pressure across the shear zone is parameterized in terms of pressure at the center p_c at $y = 0$ and the pressure at the shear zone boundaries where the poroelastic bulk meets the shear zone, that is, $p^{\pm}$ at $y = \epsilon^{\pm}$. We can explicitly write out the assumed pore pressure profile as:

$$\begin{aligned} p(y) =& \frac{y}{\epsilon}(p^{+} - p_c) + p_c \quad \text{if } 0 < y < \epsilon \\ p(y) =& \frac{y}{\epsilon}(p_c - p^{-}) + p_c \quad \text{if } -\epsilon < y < 0. \end{aligned} \tag{9}$$

Thus equating the fluid mass flux into the shear zone and in the the bulk, and vice versa, gives rise to a pressure gradient boundary condition:

$$\left.\frac{dp^{\pm}}{dy}\right|_{y=0^{\pm}} = \pm\frac{\kappa_{cy}}{\kappa}\frac{(p^{\pm} - p_c)}{\epsilon}, \tag{10}$$

where κ_{cy} is the shear zone mobility in the y direction and κ is the poroelastic bulk mobility which is rated to the bulk hydraulic diffusivity by $c = M\kappa$. We note that boundary conditions for the bulk are applied at $y = 0^{\pm}$ but in the description of the shear

zone we treat it as a finite layer with thickness between $y = \pm\epsilon$. This is because we take a boundary layer approach (similar to Appedix B of Rudnicki & Rice, 2006) where the inner solution, the shear zone, is assumed to have a finite thickness. However, the outer solution, the bulk, approximates the layer as having an infinitesimal thickness. Thus the assumption that any variation along the length of the shear zone occurs over a length scale much smaller than ϵ is implicit. In other words, we always require that $\epsilon k \ll 1$, with k representing the wavenumber (inverse of a wavelength) of any field that varies along the x-dimension.

2.2 Frictional properties

As in Heimisson et al. (2021) we represent the frictional strength of the layer in an averaged sense.

Let us assume that the frictional strength of every point in the layer can be represented as follows:

$$\frac{\tau(x,t)}{\sigma(x,t) - p(x,y,t)} = f(x,y,t) \quad \text{for } -\epsilon < y < \epsilon, \tag{11}$$

where $\tau(x,t)$ is the sum of all contributions to the shear stress, both initial background value and slip contributions. We note that the shear stress is assumed to be spatially constant across the layer. Similarly, $\sigma(x,t)$ represents background initial effective normal stress (normal stress minus the ambient pore pressure) in addition to the slip induced changes in normal stress and we assume is spatially constant across the layer. However, we have separated from the description the perturbations in pore pressure $p(x,y,t)$ since, as previously discussed, they cannot be assumed to be constant in y. Using equation (9) and averaging over the layer, we obtain:

$$\tau \frac{(p_c - p^+)\log\left(\frac{\sigma - p^-}{\sigma - p_c}\right) + (p_c - p^-)\log\left(\frac{\sigma - p^+}{\sigma - p_c}\right)}{2(p_c - p^-)(p_c - p^+)} = \langle f \rangle, \tag{12}$$

with the $\langle f \rangle$ representing the frictional coefficient of the layer. We have explored using the equation above for modeling the interface frictional strength, but we find that it renders very similar results as an linearized approximation valid in the limit of the pore pressure changes being small compared to the background normal stress:

$$\tau = (\sigma - \langle p(t) \rangle)\langle f \rangle, \tag{13}$$

where $\langle p(t) \rangle$ is the average pressure across the layers and can be computed directly

$$\langle p \rangle = \frac{1}{2\epsilon} \int_{-\epsilon}^{\epsilon} p(y) dy = \frac{1}{2} \left(p_c + \frac{p^+ + p^-}{2} \right). \tag{14}$$

Equation (13) further offers a simpler interpretation of the role of the pore pressure in the effective normal stress compared to equation (12), which helps in understanding the simulation results.

We interpret the averaged friction coefficient $\langle f \rangle$ of the shear zone as being represented by the rate-and-state friction law (e.g., Dieterich, 1979; Ruina, 1983; Marone, 1998):

$$\langle f \rangle = \frac{1}{2\epsilon} \int_{-\epsilon}^{\epsilon} f(x, y, t) dy = a \text{arcsinh} \left[\frac{V}{2V_0} \exp \left(\frac{f_0 + b \log(V_0 \theta / L)}{a} \right) \right], \tag{15}$$

where we use the regularized form of the friction law that is also valid for slip speeds V much smaller than the reference slip speed V_0 (Rice & Ben-Zion, 1996; Ben-Zion & Rice, 1997; Lapusta et al., 2000). Here a and b are constitutive parameters that describe the rate dependence and state dependence of friction, respectively. Further, f_0 is the reference coefficient and L is the characteristic slip distance over which the state evolves. The state variable is described by the aging law (Ruina, 1983):

$$\frac{d\theta}{dt} = 1 - \frac{\theta V}{L} \tag{16}$$

We note that here we have introduced a minor difference compared to (Heimisson et al., 2021). We represent friction using the regularized friction law whereas the non-regularized version was discussed by (Heimisson et al., 2021). In the linearized analysis treated by Heimisson et al. (2021), there is no difference between the two versions.

2.3 Shear Zone

Here we analyze the fluid and solid constituent mass balance of the shear zone gouge. This analysis is largely based on Heimisson et al. (2021) although here we introduce new physical processes into fluid mass balance, which are detailed below. Heimisson et al. (2021)

linearized all relations around steady-state sliding, which is needed for the purpose of linearized stability analysis. While not strictly needed for a numerical algorithm, we will here also linearize and neglect non-linear terms that arise for various reasons. Firstly, this is done because we have adapted linear compressibility relationships, as is commonly done, for the fluid, solid and pore-space. Thus for consistency, all terms should be linearized. Second, some non-linear terms have a ϵk scaling, which is by definition a small parameter. Third, since we adopt a boundary layer treatment of the shear zone with averaging in y over the thickness of the layer, the non-linearity prevents such averaging from being carried out analytically and largely negates the computational benefits from the boundary layer treatment.

2.3.1 Fluid mass balance

While other governing equations presented here are identical to those derived and used by Heimisson et al. (2021), we will introduce two additional physical processes to the fluid mass balance of the shear zone. We will thus re-derive the fluid mass balance. The two processes incorporate an injection or source term and allow for along shear zone lateral diffusion.

Within the shear zone, we state the fluid mass balance:

$$\frac{\partial m}{\partial t} + \frac{\partial q_y}{\partial y} + \frac{\partial q_x}{\partial x} = \frac{\partial}{\partial t}(Q(x,t)), \tag{17}$$

where m is the fluid mass content and q_y is fluid mass flux perpendicular to the fault (y-axis) and q_x is the fluid mass flux parallel to the fault (x-axis). $Q(x,t)$ is the cumulative fluid mass injected per unit volume of the shear zone

We note that $m = \rho_f n$, where ρ_f is fluid density and $n = n^e + n^p$ is the sum of elastic and plastic void volume and thus

$$\dot{m} = \dot{\rho}_f n + \rho_f \dot{n}. \tag{18}$$

Following Heimisson et al. (2021) we linearize $\dot{n}^e = \phi(\beta_n^p \dot{p} - \beta_n^\sigma \dot{\sigma})$ and $\dot{\rho}_f = \rho_{fo}(\beta_f^p \dot{p} + \beta_f^\sigma \dot{\sigma})$, where β_f^p and β_n^p are fluid and elastic void compressibilities respectively and $\sigma > 0$ means increased compression, also know as "the compression positive" convention. The reference compressibilities are defined at the reference void volume fraction ϕ and fluid

density ρ_{fo}. We assume the reference void volume fraction is the same as the porosity. Similarly, we assume plastic void fraction is equal to the plastic porosity: $n^{pl} = \phi^{pl}$. Thus equation (18) becomes:

$$\dot{m} = \rho_{fo}\phi(\beta_f^p\dot{p} + \beta_f^\sigma\dot{\sigma}) + \rho_{fo}\phi(\beta_n^p\dot{p} - \beta_n^\sigma\dot{\sigma} + \dot{\phi}^{pl}/\phi). \tag{19}$$

Darcy's law provides the following linearization:

$$q_x = -\rho_{fo}\kappa_{cx}\frac{\partial p}{\partial x} \tag{20}$$

where κ_{cx} is the mobility (permeability over dynamic viscosity) for fluid flux along the x-axis within the shear zone and is assumed to be spatially constant with respect to x.

Combining equations (17), (19), and (20) and integrating with respect to the y-axis gives

$$2\epsilon\rho_{fo}\phi\left[(\beta_f^p + \beta_n^p)\langle\dot{p}\rangle + (\beta_f^\sigma - \beta_n^\sigma)\dot{\sigma} + \langle\dot{\phi}\rangle^{pl}/\phi)\right] + q_y^+ - q_y^- - 2\epsilon\rho_{fo}\kappa_{cx}\frac{\partial^2\langle p\rangle}{\partial x^2} = 2\epsilon\dot{Q}(x,t) \tag{21}$$

where the source terms Q is assumed constant with respect to y.

Inserting for the fluid mass flux in y direction given a linear pressure distribution in the shear zone (equations (10) and (9)) provides:

$$\langle\dot{p}\rangle + \frac{\beta_f^\sigma - \beta_n^\sigma}{\beta_f^p + \beta_n^p}\dot{\sigma} = -\frac{\langle\dot{\phi}\rangle^{pl}}{\phi(\beta_f^p + \beta_n^p)} + \frac{\kappa_{cy}}{\epsilon^2\phi(\beta_f^p + \beta_n^p)}(\frac{1}{2}(p^+ + p^-) - p_c) + \frac{\kappa_{cx}}{\phi(\beta_f^p + \beta_n^p)}\frac{\partial^2\langle p\rangle}{\partial x^2} + \frac{\dot{Q}(x,t)}{\rho_{fo}\phi(\beta_f^p + \beta_n^p)}. \tag{22}$$

We have thus derived an equation that relates average pressure, normal stress, dilatancy, along shear zone diffusion, and fluid mass injection. The inelastic changes in porosity ϕ^{pl} is taken as

$$\langle\phi\rangle^{pl} = \phi_0^{pl} - \gamma\log\left(\frac{V_0\theta}{L}\right), \tag{23}$$

based on Segall and Rice (1995) and Segall et al. (2010), which proposed that the inelastic porosity is a function of the frictional state variable $\phi^{pl}(\theta)$. Recently this idea has gained more observational support (Proctor et al., 2020). Further, we assume that the frictional state variable θ describes the average porosity change in the shear layer.

Before implementing equation (22) numerically, we analytically integrate to obtain

$$\langle p\rangle + \frac{\beta_f^\sigma - \beta_n^\sigma}{\beta_f^p + \beta_n^p}\sigma = \frac{1}{\phi(\beta_f^p + \beta_n^p)}\left(\frac{Q(x,t)}{\rho_{fo}} - \langle\phi\rangle^{pl} + \int_0^t \frac{\kappa_{cy}}{\epsilon^2}(\frac{1}{2}(p^+ + p^-) - p_c) + \kappa_{cx}\frac{\partial^2\langle p\rangle}{\partial x^2}dt'\right), \tag{24}$$

where it is assumed that all fields are 0 at $t = 0$

2.3.2 Solid gouge constituent mass balance

We use the same solid constituent mass balance as in Heimisson et al. (2021) to obtain a constitutive relationship for fault perpendicular displacements:

$$\dot{\delta}_y = 2\epsilon\left(\frac{\phi}{1-\phi}\beta_n^p - \beta_g^p\right)\left[\langle\dot{p}\rangle - \frac{\left(\frac{\phi}{1-\phi}\beta_n^\sigma + \beta_g^\sigma\right)}{\left(\frac{\phi}{1-\phi}\beta_n^p - \beta_g^p\right)}\dot{\sigma}\right] + 2\epsilon\frac{\langle\dot{\phi}\rangle^{pl}}{1-\phi}. \tag{25}$$

Assuming that at $t = 0$ the fault is in pressure equilibrium and steady-state sliding, such that no net dilatancy or compaction occurs, then the equation can be integrated

$$\delta_y = 2\epsilon\left(\frac{\phi}{1-\phi}\beta_n^p - \beta_g^p\right)\left[\langle p\rangle - \frac{\left(\frac{\phi}{1-\phi}\beta_n^\sigma + \beta_g^\sigma\right)}{\left(\frac{\phi}{1-\phi}\beta_n^p - \beta_g^p\right)}\sigma\right] + 2\epsilon\frac{\langle\phi\rangle^{pl}}{1-\phi}. \tag{26}$$

3 Solutions for Coupled Shear Zone and Bulk

In this section we define the joint Fourier-Laplace transform

$$\bar{\hat{\delta}}_x(s,k) = \int_0^\infty\int_{-\infty}^\infty \delta_x(t,x)e^{-ikx-st}dxdt, \tag{27}$$

applied here in the slip $\delta_x(x,t)$, or displacement discontinuity across the layer in the x direction, where the bar symbol represents the Laplace transform in time and the hat the Fourier transform along the x spatial axis. Some symbols may not carry the hat symbol if they are explicitly written out in term in terms of the wavenumber k.

As in Heimisson et al. (2021), we follow the procedure outlined by Heimisson et al. (2019). In particular, we derive solutions in the Fourier-Laplace domain for shear stress, pore pressure, and normal stress change at the slip surface ($y \to 0^\pm$). As provided by Heimisson et al. (2021) the relationships between change in shear stress $\bar{\hat{\tau}}'$, pore pres-

sure change on either side of the layer $\bar{\hat{p}}^{\pm}$, and change in total normal stress $\bar{\hat{\sigma}}_{yy}$ in terms of $\bar{\hat{\delta}}_x$, $\bar{\hat{\delta}}_y$, and $\bar{\hat{p}}_c$ are given by the following equations:

$$\bar{\hat{\tau}} = -\frac{G|k|\bar{\hat{\delta}}_x}{2(1-\nu_u)}\bar{H}_1(s,k) \tag{28}$$

and

$$\bar{\hat{p}}^{\pm} = \mp\frac{ikGB\bar{\hat{\delta}}_x}{3}\frac{1+\nu_u}{1-\nu_u}\bar{H}_2(s,k) - \bar{\hat{p}}_c\frac{\mathcal{F}}{\mathcal{F}+1}\left(\bar{H}_2(s,k)-1\right) + \frac{|k|GB\bar{\hat{\delta}}_y}{3}\frac{1+\nu_u}{1-\nu_u}\bar{H}_2(s,k), \tag{29}$$

and

$$\bar{\hat{\sigma}}_{yy} = \bar{\hat{p}}_c\frac{3}{2B(1+\nu_u)}\frac{\mathcal{F}}{\mathcal{F}+1}(\bar{H}_1(s,k)-1) - \frac{G|k|\bar{\hat{\delta}}_y}{2(1-\nu_u)}\bar{H}_1(s,k), \tag{30}$$

where

$$\bar{H}_1(s,k) = 1 - \frac{2(\nu_u-\nu)}{1-\nu}\frac{ck^2}{s}\frac{1+\mathcal{F}}{\mathcal{F}+\sqrt{1+s/ck^2}}\left(\sqrt{1+s/ck^2}-1\right), \tag{31}$$

and

$$\bar{H}_2(s,k) = \frac{\sqrt{1+s/ck^2}-1}{\sqrt{1+s/ck^2}+\mathcal{F}}. \tag{32}$$

$\mathcal{F}$ is a dimensionless group that characterizes the importance of flux across the fault:

$$\mathcal{F} = \frac{\kappa_{cy}}{\kappa}\frac{1}{|k|\epsilon}. \tag{33}$$

We now seek to invert the Laplace transform. We define

$$\bar{K}_1 = \bar{H}_1 - 1 \text{ and } \bar{K}_2 = \bar{H}_2 - 1. \tag{34}$$

As was shown by Heimisson et al. (2019), $\bar{H}_1$ and $\bar{H}_2$ approach unity in the limit of short time or negligible diffusion, which reduces Eqs. (28), (29), and (30) to their corresponding undrained limits. $\bar{K}_1$ and $\bar{K}_2$ thus represent the transient changes in shear stress and pore pressure on the fault that arise due to pore pressure diffusion.

We note that $\bar{H}_1 = 1 - 2(\nu_u - \nu)/(1-\nu)(1+\mathcal{F})(ck^2/s)\bar{H}_2$. Thus in the time domain the inverse transform of $\bar{H}_1$ is closely related to the time integral of the inverse transform of $\bar{H}_2$. Using the convolution theorem for Laplace transforms we find that Eqs. (28) and (29) take the form:

$$\hat{\tau}' = -\frac{G|k|}{2(1-\nu_u)}\left(\hat{\delta}_x + \int_0^t \hat{\delta}_x(t')K_1(t-t',k)dt'\right), \tag{35}$$

$$\hat{p}^{\pm} = \mp\frac{ikGB}{3}\frac{1+\nu_u}{1-\nu_u}\left(\hat{\delta}_x + \int_0^t \hat{\delta}_x(t')K_2(t-t',k)dt'\right) - \frac{\mathcal{F}}{\mathcal{F}+1}\int_0^t \hat{p}_c(t')K_2(t-t',k)dt' + \frac{|k|GB}{3}\frac{1+\nu_u}{1-\nu_u}\left(\hat{\delta}_y + \int_0^t \hat{\delta}_y(t')K_2(t-t',k)dt'\right). \tag{36}$$

and

$$\hat{\sigma}_{yy} = \frac{3}{2B(1+\nu_u)}\frac{\mathcal{F}}{\mathcal{F}+1}\int_0^t \hat{p}_c(t')K_1(t-t',k)dt' - \frac{G|k|}{2(1-\nu_u)}\left(\hat{\delta}_y + \int_0^t \hat{\delta}_y(t')K_1(t-t',k)dt'\right) \tag{37}$$

We have thus separated the undrained response and the transient diffusion behavior. This behavior characterized by the convolution kernels K_1 and K_2 that represent the inverse Laplace transforms of K_1 and K_2 respectively. In other words $K_1(t) = \mathcal{L}^{-1}\left\{\bar{K}_1\right\}(t)$ and $K_2(t) = \mathcal{L}^{-1}\left\{\bar{K}_2\right\}(t)$.

Analytical expressions for K_1 and K_2 can be attained through repeated application of the convolution theorem to separate $\bar{K}_1$ and $\bar{K}_2$ into factors of known inverse Laplace transforms.

$$K_1(t,k) = -\frac{2(\nu_u-\nu)}{1-\nu}ck^2(1+\mathcal{F})\left(1 + \frac{1}{\mathcal{F}-1}\left[\mathcal{F}e^{(\mathcal{F}^2-1)ck^2t}\mathrm{erfc}\left(\mathcal{F}\sqrt{ck^2t}\right) - \mathcal{F} + \mathrm{erf}\left(\sqrt{ck^2t}\right)\right]\right) \tag{38}$$

$$K_2(t,k) = -ck^2(1+\mathcal{F})\left[\frac{e^{-ck^2t}}{\sqrt{\pi ck^2t}} - \mathcal{F}e^{(\mathcal{F}^2-1)ck^2t}\mathrm{erfc}\left(\mathcal{F}\sqrt{ck^2t}\right)\right]. \tag{39}$$

We note that kernel K_2 is singular when $t \to 0$. However, this is an integrable singularity and the convolution kernel can be integrated in the sense of taking a Cauchy principal value.

In summary, equations (35), (36), and (37) represent analytical solutions for the shear stress, pore pressure (at shear zone boundary), and normal stress given a time-history of slip δ_x, opening δ_y and/or shear zone center pore pressure p_c which have been transformed in the wavenumber (Fourier) domain. Alternatively, these expressions represent analytical solutions for a single plane wave perturbation in slip δ_x, δ_y and/or p_c of generic form $f(t)\exp(ikx)$, where $f(t)$ is some time-dependent function. In section 4.1 we use this property to construct general solutions for arbitrary histories of slip δ_x, opening δ_y and/or shear zone center pore pressure p_c.

4 Numerical Method

4.1 Fourier series representation of poroelastic relations

We represent δ_x, δ_y and p_c as a Fourier series

$$\delta_x(x,t) = \sum_{n=-N/2}^{N/2-1} D_{x,n}(t)e^{ik_n x}, \quad k_n = \frac{2\pi n}{\lambda}, \tag{40}$$

$$\delta_y(x,t) = \sum_{n=-N/2}^{N/2-1} D_{y,n}(t)e^{ik_n x}, \quad k_n = \frac{2\pi n}{\lambda}, \tag{41}$$

and

$$p_c(x,t) = \sum_{n=-N/2}^{N/2-1} P_n(t)e^{ik_n x}, \quad k_n = \frac{2\pi n}{\lambda}, \tag{42}$$

where N is even and equal to the number of points at which $\delta(x,t)$ and $p_c(x,t)$ are evaluated, λ represents the length of the simulation domain. The Fourier transform is given by

$$\hat{\delta}_x(k,t) = \sum_{n=-N/2}^{N/2-1} 2\pi D_{x,n}(t)\delta_D(k-k_n), \tag{43}$$

and corresponding relations exist for $\hat{p}_c$ and $\hat{\delta}_y$ where δ_D is the Dirac delta function. Inserting the transformed series into equations (35), (36) , and (37) and performing the trivial inverse Fourier transforms provide

$$\tau' = -\frac{G}{2(1-\nu_u)} \sum_{n=-N/2}^{N/2-1} |k_n| \left(D_{x,n}(t) + \int_0^t D_{x,n}(t')K_1(t-t',k_n)dt' \right) e^{ik_n x}, \tag{44}$$

$$p^{\pm} = \sum_{n=-N/2}^{N/2-1} \left(\mp \frac{iGB}{3} \frac{1+\nu_u}{1-\nu_u} k_n \left[D_{x,n}(t) + \int_0^t D_{x,n}(t') K_2(t-t', k_n) dt' \right] + \dots \right.$$
$$\frac{GB}{3} \frac{1+\nu_u}{1-\nu_u} |k_n| \left[D_{y,n}(t) + \int_0^t D_{y,n}(t') K_2(t-t', k_n) dt' \right] - \dots$$
$$\left. \frac{\mathcal{F}(k_n)}{\mathcal{F}(k_n)+1} \int_0^t P_n(t') K_2(t-t', k_n) dt' \right) e^{ik_n x}, \tag{45}$$

and

$$\sigma_{yy} = \frac{3}{2B(1+\nu_u)} \sum_{n=-N/2}^{N/2-1} \left(\frac{\mathcal{F}(k_n)}{\mathcal{F}(k_n)+1} \int_0^t P_n(t') K_1(t-t', k_n) dt' - \dots \right.$$
$$\left. \frac{G}{2(1-\nu_u)} |k_n| \left[D_{y,n}(t) + \int_0^t D_{y,n}(t') K_1(t-t', k_n) dt' \right] \right) e^{ik_n x} \tag{46}$$

Testing and validation revealed that the first term of the pore pressure (Eq. 45) is prone to developing the Gibbs phenomenon in the presence of steep gradients. This may stem from how the sign of the pore pressure depends on k_n and not the absolute value of $|k_n|$ as for other terms. Oscillations, such as the Gibbs phenomena, are somewhat mitigated by the diffusional nature of the pore pressure where short-wavelength oscillations diffuse rapidly. However, a much improved convergence of the series in Eq. (29) and nearly complete removal of the Gibbs phenomenon can be achieved with a Lanczos sigma factor (Duchon, 1979):

$$p^{\pm} = \sum_{n=-N/2}^{N/2-1} \left(\mp \frac{iGB}{3} \frac{1+\nu_u}{1-\nu_u} k_n \, \mathrm{sinc}\left(\frac{n}{N/2}\right) \left[D_{x,n}(t) + \int_0^t D_{x,n}(t') K_2(t-t', k_n) dt' \right] + \dots \right.$$
$$\frac{GB}{3} \frac{1+\nu_u}{1-\nu_u} |k_n| \left[D_{y,n}(t) + \int_0^t D_{y,n}(t') K_2(t-t', k_n) dt' \right] - \dots$$
$$\left. \frac{\mathcal{F}(k_n)}{\mathcal{F}(k_n)+1} \int_0^t P_n(t') K_2(t-t', k_n) dt' \right) e^{ik_n x}, \tag{47}$$

where $\mathrm{sinc}(x) = \sin(\pi x)/(\pi x)$ is the normalized sinc function. It is worth noting that an inverse FFT of the Fourier coefficients in equations 44, 45, 46, and 47 is an efficient way to compute the stresses and pore pressure at each value of x.

4.1.1 Comparison to Song and Rudnicki (2017)

To partially validate solutions in the previous section we compare to the analytical solution provided for a single edge dislocation on a leaky plane provided by Song and

Rudnicki (2017) (Figure 2). In the problem analyzed by Song and Rudnicki (2017) $\delta_x = \mathcal{H}(t)\mathcal{H}(-x)$, $\delta_y = 0$, $p_c = 0$, in which case $\sigma_{yy} = 0$. We use equations (44) and (47) after retrieving Fourier series coefficients using a fast Fourier transform (FFT) algorithm of $\delta_x = \mathcal{H}(t)\mathcal{H}(-x)$ evaluated on a domain size ranging from $x = -50$ to $x = 50$ m. Comparison in Figure 2 reveals excellent agreement between the two approaches.

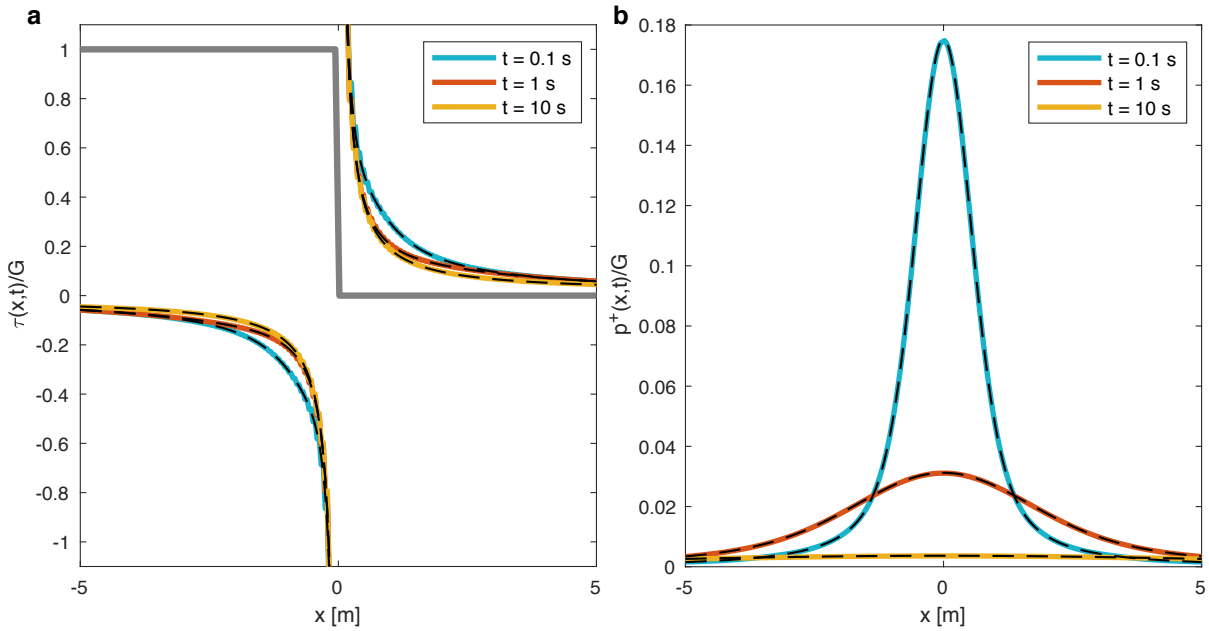

Figure 2. Comparison of equations (44) and (47) to equations (A1) and (72) respectively in Song and Rudnicki (2017). Colored lines represent the spectral boundar-integral solution and overlapping dashed black lines represent the Song and Rudnicki (2017) solution. **a** Shear stress normalized by shear modulus G near the dislocation edge (indicated in gray) of unit slip amplitude at three different times, which span approximately the undrained, drained limits as well as an intermediate stage. **b** pore pressure due to the same edge dislocation. Results are shown for $c = 1$ m^2/s, $B = 0.5$, $\kappa_c/(\kappa\epsilon) = 1$ m^{-1}, $\nu = 0.15$, $\nu_u = 0.45$.

4.2 Time-stepping

Here we describe the time-stepping scheme to simulate slow and fast slip with dilatancy and fluid injection into the faults. The scheme builds on the predictor-corrector schemes of Lapusta et al. (2000) and Heimisson (2020). However, several significant modifications have been introduced to resolve fluid diffusion. Below we shall describe the stages

of a single time-step by the algorithm. We also refer the reader to the source code (Heimisson, 2022) for a more explicit implementation of the time-stepping scheme.

1. Initial explicit Euler prediction is made for time $t^{n+1} = t^n + \Delta t$ for δ_x^*, δ_y^*, p_c^*, V^*, where the asterisk represents the prediction of the next time-step.
2. Fourier coefficients are computed corresponding to the prediction values δ_x^*, δ_y^*, p_c^*, that is $D_{x,n}^*$, $D_{y,n}^*$, P_n^* using a Fast-Fourier Transform (FFT).
3. Using equations (44), (46), and (47) the Fourier coefficients for changes in shear stress, normal stress and boundary pore pressure are computed and an inverse FFT is used to sum all Fourier modes.
4. Prediction for shear stress τ^* and effective normal stress $(\sigma - p)^*$ is computed. In the results, we use the average pore pressure $\langle p \rangle$; however, we note that p could here represent any number of pore pressure values, e.g. $p^{\pm}$ or p_c, depending on what assumptions are made about the relevant pore pressure in the shear localization region. In our numerical implementation (Heimisson, 2022), the user sets which pore pressure to use.
5. Prediction of the updated state-variable is computed using the analytical integration of the aging law by Kaneko et al. (2011) which is assumes constant slip speed from t to $t + \Delta t$

$$\theta^* = \theta^p \exp\left(-\frac{\Delta t}{2L}(V^n + V^*)\right) + \frac{2L}{(V^n + V^*)}\left(1 - \exp\left(-\frac{\Delta t}{2L}(V^n + V^*)\right)\right), \quad (48)$$

where we have taken taken the slip speed as the average $(V^p + V^*)/2$ between the slip speed at time t^n and $t^{n+1} = t^n + \Delta t$. Here we use the superscript ^{n} to represent the fields at the previous time step, that is at time t^n.

6. Via an algebraic manipulation of the rate-and-state friction law (13) and (15) a correction for the slip speed is computed

$$V^{**} = 2V_0 \sinh\left(\frac{\tau^* - \eta V^*}{a(\sigma - p)^*} \exp\left(-f_0/a - \frac{b}{a}\log(V_0\theta^*/L)\right)\right). \quad (49)$$

However, for locations along the fault where the slip speed exceeds a threshold value (here set to 1 cm/s) the previous expression is found to lead to numerical dispersion and the slip speed is obtained by solving the following non-linear equation as done by Heimisson (2020):

$$\left| V^{**} - 2V_0 \sinh\left(\frac{\tau^* - \eta V^*}{a(\sigma - p)^*} \exp\left(-f_0/a - \frac{b}{a}\log(V_0\theta^*/L)\right)\right)\right| = 0. \tag{50}$$

7. Using the new slip speed correction V^{**} the state variable is also updated

$$\theta^{**} = \theta^p \exp\left(-\frac{\Delta t}{2L}(V^n + V^{**})\right) + \frac{2L}{(V^n + V^{**})}\left(1 - \exp\left(-\frac{\Delta t}{2L}(V^n + V^{**})\right)\right), \tag{51}$$

and from equation (23) $\langle\phi\rangle_{pl}^{**}$ is computed using θ^{**}.

8. Updating p_c: for the sake of brevity, we will only refer to the code (Heimisson, 2022), see also data availability statement, for a detailed implementation of this time-step, but a summary follows. In equation (24) (after substituting with equation (14) for $\langle p\rangle$) we approximate the $\partial^2/\partial x^2$ derivative with second-order finite difference approximation. The time-integral is discretized using a trapezoidal rule. Predictions from step 1 and 3 are used to compute the various fields at time t^{n+1} except we solve for p_c^{**} (the prediction of p_c for time t^{n+1}) implicitly by solving a system of linear equations.
9. Finally p_c^{**} is used to update δ_y^{**}, $\langle p\rangle^{**}$, and $\delta_x^{**} = \delta_x^n + \Delta t(V^n + V^{**})/2$.

After the steps above, the algorithm determines if it will proceed to the next time-step or reiterate following these rules.

- A minimum of one iteration is used. If the algorithm finishes the aforementioned steps for the first time at the current time then it must iterate again. The algorithm moves back to step 1, but instead of explicit guesses for the new time step it uses previous updates. That is $\delta_x^{**} \to \delta_x^*$, $\delta_y^{**} \to \delta_y^*$, and $p_c^{**} \to p_c^*$.
- If a minimum one iteration has been done, the algorithm checks for absolute and relative error in the estimate of p_c. That is if $\max(|p_c^{**} - p_c^*|)/(a\sigma_0) > \xi/10$ (where a is the direct effect parameter) or $||p_c^{**} - p_c^*||_1/||p_c||_1 > \xi/10$ is violated then a new time-step is selected $\Delta t \to \Delta t/2$ and the algorithm proceeds to step 1 using the following initial predictions $(\delta_x^{**} + \delta_x^n)/2 \to \delta_x^*$, $(\delta_y^{**} + \delta_y^n)/2 \to \delta_y^*$, and $(p_c^{**} + p_c^n)/2 \to p_c^*$. Here ξ is a factor that controls the accuracy of the solution, in simulations shown later this is set to $\xi = 1/32$, see Appendix B for more discussion of ξ.
- If both a minimum of one iteration has been carried out and the error tolerances are satisfied, the algorithm proceeds to a new time step and ** predictions are as-

signed as field values are time t^{n+1}. Finally, the new initial time-step is selected $\Delta t \rightarrow \min(\xi V^{n+1}/L, 1.1 \cdot \Delta t)$ where first we make sure that the state evolution is well resolved, by picking ξ sufficiently small. Second, we make sure not to grow the time-step too much if the pore pressure evolution requires a smaller time-step than indicated by $\xi V^{n+1}/L$.

4.3 Convolution kernel computation and truncation

Alongside with the time stepping, which was described in the previous section, we update and calculate the convolution in equations (44), (46), and (47). In computing the convolution we first compute a kernel values at lag times t_i for each wavenumber k_n i.e. $K_1(t_i, k_n)$ and $K_2(t_i, k_n)$, where t_i is selected to span a time interval from $\zeta_l \min(t_b, t_f)$ to $\zeta_u \min(t_b, t_f)$. In practice we take $\zeta_l = 10^{-6}$ and $\zeta_u = 20$ and t_b and t_f are the diffusion time-scales of the bulk and of the flux through the shear zone:

$$t_b = \frac{1}{ck^2}, \tag{52}$$

and

$$t_f = \frac{1}{\mathcal{F}^2 c k^2} = \frac{\kappa^2 \epsilon^2}{\kappa_c^2 c}. \tag{53}$$

We thus evaluate the convolution kernels between a time that is negligible compared to the diffusional time-scales $\zeta_l \min(t_b, t_f)$, up to a time that is long compared to the diffusional time scales $\zeta_u \min(t_b, t_f)$. Evaluation points t_i are selected by combining both points at a linearly equally spaced times, and logarithmically equally spaced times. Here we use 1024 evaluation points, but we found for in some cases, such as the benchmarking against the linear stability analysis of Heimisson et al. (2021) that much fewer evaluation points were needed.

Since we pre-compute the convolution kernels we need to determine the values of the Fourier coefficients $D_{x,n}$, $D_{y,n}$, P_n at times $t - t_i$. This is done by storing the Fourier coefficients' values at selected times and then determining their values at the convolution times t_i by linear interpolation.

The criteria for storing a Fourier coefficient value are implemented by setting an integer N_{st}, which is the maximum number of time-steps that can be taken without storing the Fourier coefficients. We compute

$$N_{st} = \left\lfloor \min(1 + \min(t_f, t_b)/\Delta t; 1 + \min(a\sigma_0/(p_c^n - p_c^{lst}))/20; N_{st}^{\max}) \right\rfloor , \tag{54}$$

where p_c^{lst} is the vector of p_c values when the Fourier coefficients were last stored and $N_{st}^{\max}$ is some user-determined value that makes sure the coefficients are sampled at least every $N_{st}^{\max}$ time-step. The first criterion in the equation makes sure that the minimum diffusion time is resolved in the stored Fourier coefficients and thus changes the Fourier coefficients that occur on time scales relevant for diffusion are stored. Testing has suggested that under-sampling here may not be an issue since the shortest diffusion times correspond to the largest wavenumbers (shortest wavelengths) and if the simulation is well resolved, then the influence of these wavelengths is negligible. The second criterion makes sure that if the pore pressure is changing rapidly, then information of these rapid changes is stored in the stored coefficients. This is particularly important for injection problems. However, for efficiency we overwrite the value above for N_{st} if $t^n - t^{lst} < \zeta_l \min(t_b, t_f)$, where t^{lst} is the time when the coefficients were last stored, in which case we set $N_{st} = N_{st}^{\max}$. This makes sure that we do not store coefficients over time scales too short for any diffusional process to occur. This makes the seismic phase of the simulations much more efficient.

5 Application

Here we show an application of the code. We compare the code to the Guglielmi et al. (2015) experiment, in which fluid was injected into a shallow fault and slip and pressure were monitored. The slip and pressure data was previously analyzed by Larochelle et al. (2021a) by modeling 1D diffusion in a plane strain linear elastic bulk with rate-and-state friction. We use their parameter estimates (see also table A1) and their simplified pore pressure history (see Figure 2 in Larochelle et al., 2021a) as input, but we vary other processes and parameters that were not accounted for by Larochelle et al. (2021a), or in most comparable studies, such as dilatancy, different permeabilities of the bulk compared to the shear zone, and poroelastic parameters. Specifically, we explore a set of parameters where the dilatancy coefficient takes values $\gamma = 0$, $1.7{\cdot}10^{-5}$, and $1.7{\cdot}10^{-4}$. Further, the bulk hydraulic diffusivity is $c = 4{\cdot}10^{-8}$ or $4{\cdot}10^{-7}$ m^2/s and the undrained Pois-

son's ratio is ν =0.35 or 0.262. We note further discussion of parameters in Appendix A.

We follow the setup and initial conditions as implemented by Larochelle et al. (2021a). However, some critical differences in model setup and characterization of fluid flow are worth mentioning. Larochelle et al. (2021a) implement 1D isotropic diffusion, meaning the pressure in the bulk and shear zone is spatially constant in y, and no fluid-solid coupling of the bulk. This implies isotropic diffusivity across the shear zone and bulk and that the bulk is purely elastic, thus no coupling of fluid flow and deformation. Here we can create an elastic bulk response by selecting the hydraulic diffusivity as either very large or very small (drained and undrained conditions, respectively). However, this would make the bulk extremely diffusive or impermeable, which is then inconsistent with Larochelle et al. (2021a) where bulk diffusion is relevant at the time scale of nucleation. This incompatibility, along with some other critical differences, makes the direct comparison of results most likely impossible. Here we assume that the pressure measured in the experiment Guglielmi et al. (2015) reflects the shear zone center pressure p_c, whereas in Larochelle et al. (2021a) this would be a constant value along the y-dimension at $x = 0$.

We stress that the goal here is neither to replicate the simulations and results Larochelle et al. (2021a) nor to model the experiments of Guglielmi et al. (2015) explicitly. Here the goal is to use these previous results to guide us in finding the approximately right part of the parameter space and be consistent with experimental values. Then we wish to vary other properties that are generally not tested in comparable studies to understand if they significantly affect the slip process and nucleation during injection.

5.1 Reference case, no dilatancy

First, we explore the simplest case, and the one most studied in the literature, where pore pressure change in the shear zone is introduced only by injection and does not cause pressure change through dilatancy. In most cases, this would mean that the pore pressure change is one-way coupled. In other words, the pore pressure changes slip by affecting the frictional strength, but the slip does not change the pore pressure (e.g. Bhattacharya & Viesca, 2019; Cappa et al., 2019; Larochelle et al., 2021a). However, in our case, this is not true due to the poroelastic coupling. For example, the fault pressurization changes

579 δ_y, which causes compaction of the host rock and this changes pore pressure adjacent
580 to the shear zone.

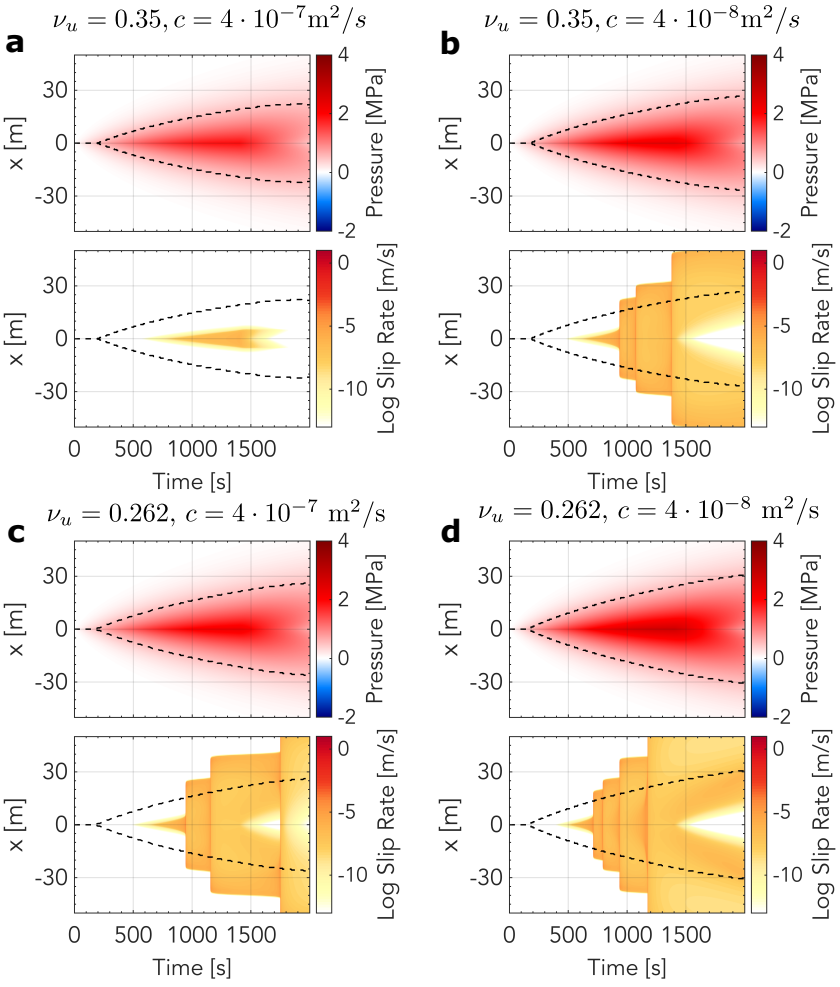

Figure 3. Simulations of fault fields with time and no dilatancy $\gamma = 0$ but varied bulk diffusivity c and undrained Poisson's ratio ν_u as is listed above each panel. Each panel shows the average shear zone pressure $\langle p \rangle$ and log slip rate $\log_{10} V$. x indicates location along the length of the fault, but we note that the simulation domain is 5 times larger (400 m) than is shown. The black dashed lines are the 0.5 MPa pressure contours, which we take as representative of the pressure front distance. We observe highly stabilized slip in panel **a**, where the undrained Poisson's ratio and the bulk diffusivity are larger. However, highly unstable slip in panel **d** with **a** smaller undrained Poisson's ratio and bulk diffusivity (four seismic events).

The simulations without dilatancy (Figure 3) demonstrate a wide spectrum of slip stability based on two parameters that have not been explored much in the literature: bulk diffusivity and undrained Poisson's ratio. First, with larger bulk diffusivity c and undrained Poisson's ratio ν_u (panel **a**) we observe very limited slip in response to the injection. Clearly, the fault is not slipping in a seismically unstable manner. In contrast, a smaller undrained Poisson's ratio ν_u and bulk diffusivity c (panel d) result in highly unstable behavior with four seismic ruptures. In the two other cases, where one value is larger and the other smaller (panels **b** and **c**), we see similarly unstable behavior with three ruptures. This may indicate a degree of trade-off between ν_u and c, and neither parameter alone is controlling the stability characteristics of the fault. This makes sense since c will control the slip speed at which the bulk will respond in an undrained manner. We discuss how the undrained parameters play a significant role in the stability in section 6.1.

5.2 Simulations with dilatancy $\gamma = 1.7 \cdot 10^{-5}$

Here we explore the same parameter combinations, initial conditions, imposed injection, and overall setup as in Figure 3. However, we now include dilatancy setting $\gamma = 1.7 \cdot 10^{-5}$. This is 10% of the standard value of $\gamma = 1.7 \cdot 10^{-4}$, which Segall and Rice (1995) derived from the experiments of Marone et al. (1990). $\gamma = 1.7 \cdot 10^{-4}$ is typically used in the literature and results using that value will be shown in the next section. However, we decided to explore a smaller value as it reveals an intermediate regime where slow slip outpaces the diffusion front (Figure 4)

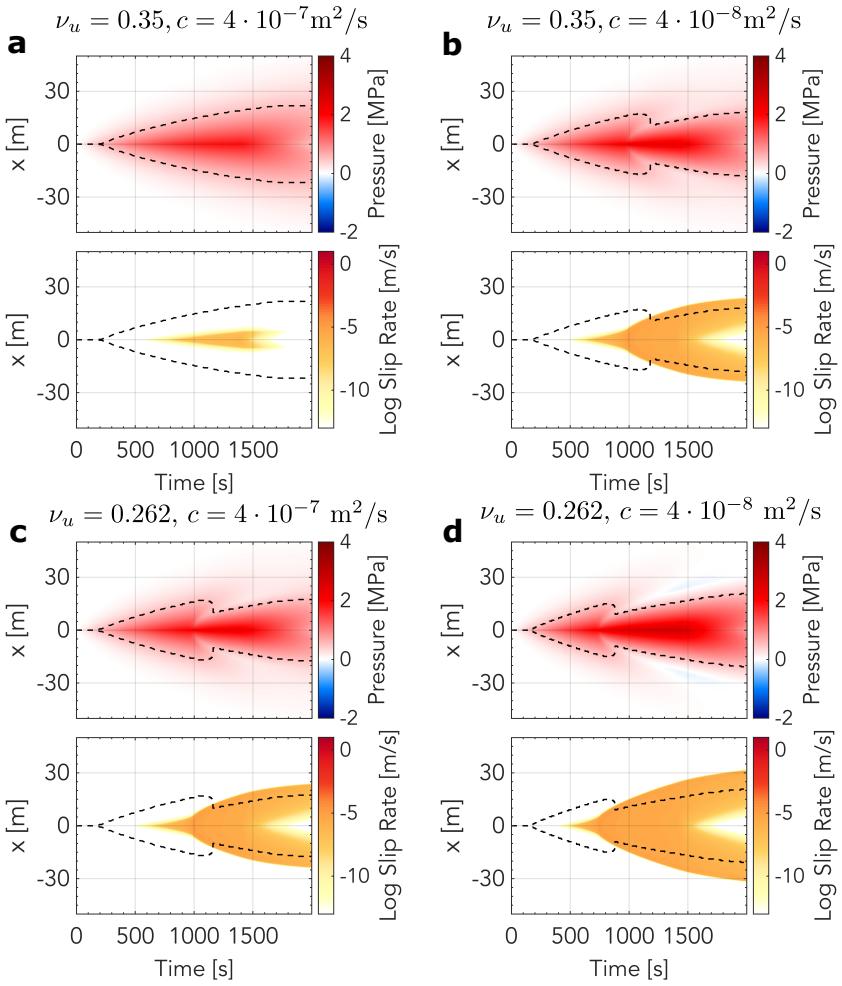

Figure 4. Simulations of fault fields with time and dilatancy $\gamma = 1.7 \cdot 10^{-5}$. Otherwise, the figures and simulation setup are the same as in Figure 3. We observe highly stabilized slip in panel a, where the undrained Poisson's ratio and the bulk diffusivity are larger. Here the results are largely consistent with those of Figure 3 where panel **a** shows very stable behavior, panel **d** is the most unstable, and parameter combinations in panels **b** and **c** show similar stability. However, here all simulations show gradual migration of a slow slip front and no seismic event. Thus all simulations are substantially stabilized, as is expected from introducing dilatancy. We note negative pore pressure change at the slip-front in panel **d**, and strong overall deviation from the square root characteristic growth of the pore pressure front.

It is notable in Figure 4 that we observe similar effect of stabilization by changing c and ν_u compared to Figure 3, with larger ν_u and c showing high degree of stabilization (panel **a**), but smaller ν_u and c a developing instability, but panels **b** and **c** have

similar levels of stability. However, in Figure 4 the style of slip is very different. We observe no seismic events but slow slip migration. In all cases, except panel a, the slow slip outpaces the pore pressure front as indicated by the dashed 0.5 MPa contour. At the same time, the slip is drastically altering the pore pressure front. The influence of dilatancy on the fault pore pressure is most prominent in panel d, where the average pressure at the rupture tip is decreased compared to a background value, i.e. negative pore pressure change. The result is not a classic square-root-of-time diffusional pressure characteristic as is seen in Figure 3 and Figure 4a but rather square-root characteristic initially, but once the slip speed is significant and the dilatancy alters the pore pressure and the characteristic is perturbed. The resulting shape of the fault pore pressure contour resembles the outline of a squid's head.

5.3 Simulations with dilatancy $\gamma = 1.7 \cdot 10^{-4}$

Finally, we carry out simulations using the value of the dilatancy coefficient $\gamma = 1.7{\cdot}10^{-4}$ as inferred by Segall and Rice (1995). This may be considered as a standard value as it is typically used. However, there is no general reason to believe that the dilatancy coefficient could not vary significantly.

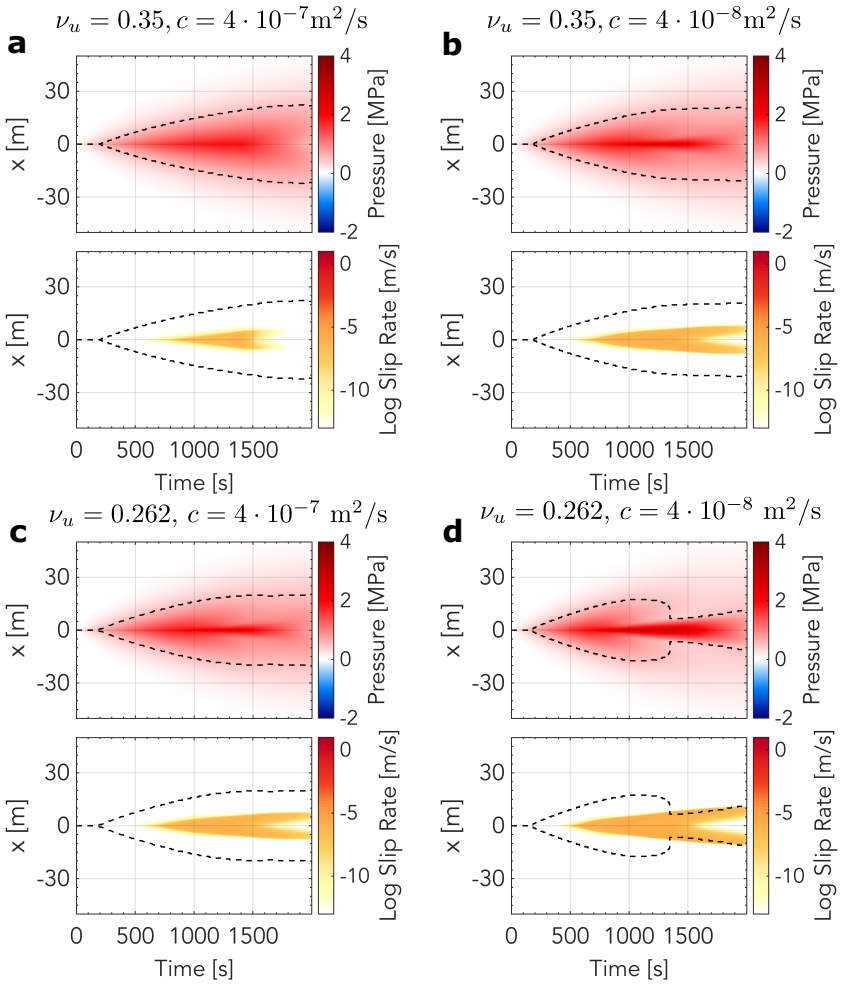

Figure 5. Simulations of fault fields with time and dilatancy $\gamma = 1.7 \cdot 10^{-4}$. Otherwise the figures and simulation setup is the same as in Figure 3. We observe highly stabilized slip in all cases. Unlike the previous two cases the rupture only grows in a region of significantly elevated pore pressure.

For $\gamma = 1.7 \cdot 10^{-4}$ we observe highly stabilized slip (Figure 5). There is no seismic rupture and no slow slip front that is growing faster than the pore pressure diffuses. In other words, the rupture is driven in the location of high pore pressure and thus grows quasi-statically with the pressure front. Dilatancy influences the fault pressure, in particular in Figure 5d, but compared to Figure 4 we observe that the dilatancy induced changes in pore pressure are less prominent in Figure 5. This may be somewhat counterintuitive given that the dilatancy coefficient is an order of magnitude larger in Figure 5. Since the dilatancy coefficient is smaller in Figure 4 a larger slip patch can de-

velop before dilatancy becomes significant. This slip patch is less stiff or alternatively one might state that it produces a higher energy release rate. Thus it is able to drive rupture propagation at a higher rate and more slip speed, which ultimately results in increased pore pressure response than when the dilatancy coefficient is larger and suppresses instability development at an earlier time. We emphasize that selecting $\gamma = 1.7 \cdot 10^{-4}$ does not generally mean stable rupture due to injection. Even if all the same parameters are selected, a seismic rupture could develop by simply altering the injection strategy; for example, injecting for a significantly longer time and at a higher rate would likely eventually lead to a seismic event.

6 Discussion

6.1 Result summary and interpretation

The application of our method has had two main themes. First, by exploring how dilatancy affects the fault response due to injection. Second, how altering the bulk diffusivity and undrained Poisson's ratio influences the fault response from injection. Dilatancy is already understood to be a stabilizing mechanism (Rudnicki & Chen, 1988; Segall & Rice, 1995; Segall et al., 2010), although limited study of coupled injection and dilatancy has been carried out (except Ciardo & Lecampion, 2019; Yang & Dunham, 2021). Thus our general finding, that fault slip is stabilized and aseismic slip is promoted when dilatancy is included is not surprising. We have thus chosen to contrast this well-known stabilizing mechanism with less explored parameters that we are uniquely positioned to investigate with the method described in this paper. Namely we vary parameters c and ν_u. Indeed the latter has meaning only for a poroelastic solid. A purely elastic solid, as considered in most studies(with some exceptions, e.g. Jha & Juanes, 2014; Torberntsson et al., 2018; Heimisson et al., 2019) has only a single Poisson's ratio.

Our selection of three different γ values reveals different modes of rupture. First, highly unstable response with repeated seismic ruptures of the same part of the fault. Second, slow slip migration that propagates beyond the pressurized region. Finally, quasi-statically growing slip only in regions of high pressure. This can be observed in Figures 3, 4, and 5 respectively. The Guglielmi et al. (2015) experiment reported primarily aseismic slip and significant dilatant behavior. Some micro-earthquakes were reported, but they may have been off the main fault and represent only a small fraction of the moment

660 released. Thus our findings show, given the experimental constraints and information
661 from a previous modeling study (Larochelle et al., 2021a) that inclusion of dilatancy re-
662 sults in behavior qualitatively similar to what was reported by Guglielmi et al. (2015).
663 However, further study is needed for quantitative matching. We highlight that the method
664 presented predicts fault opening from dilatancy or pressurization and thus may provide
665 additional constraints in data application when that is directly measured (Cappa et al.,
666 2019).

667 Our reported influence of bulk diffusivity and undrained Poisson's ratio is more novel.
668 We observe that changing the bulk diffusivity by order of magnitude significantly sta-
669 bilizes the fault in the simulations. It is important to emphasize that this result is also
670 contingent on the shear zone mobility, which we have not systematically varied. This is
671 due to the time scales of fluid diffusion in the bulk and shear zone are not independent
672 as discussed by Heimisson et al. (2021). The bulk diffusivity has an important control
673 on the stability of the fault as it will control how rapidly fluids can escape the shear zone.
674 Our parameter choice (Appendix A) is such that it reflects a fault initially far from steady-
675 state or, in other words, not critically stressed. Although the changes in average pres-
676 sure in Figures 3, 4, and 5 are subtle, they are sufficient to cause significant stabiliza-
677 tion in fault behavior. This can be observed by comparing panels **a** and **b**, or **c** and **d**
678 in Figures 3, 4, and 5.

679 Bulk diffusivity is often considered to be the same as that of the shear zone or the
680 bulk is simply taken to be impermeable. In this study, we have taken what we consider
681 to be small values of c, yet we observe a very significant effect. Further, as seen in equa-
682 tion (22) the flux into the bulk scales with κ_{cy}/ϵ^2. Since we expect ϵ the shear zone half-
683 thickness to be small, we can expect that flux into the bulk occurs rapidly. Indeed in this
684 study, we set the κ_{cx}, along shear zone mobility, to be a factor 10^9 larger than κ_{cy} such
685 that the fluid migration along the shear zone was significant compared to the flux into
686 the bulk. This highlights that how rapidly the bulk can transport fluids is critical for the
687 fault dynamics. As discussed in Heimisson et al. (2021), and can be seen in the SBI so-
688 lutions in this paper, the characteristic time of bulk diffusion is $\sim 1/(ck^2)$. Thus the bulk
689 fluid transport is highly dependent on length scale, and idealizations of an impermeable
690 bulk may only be valid at a certain length scale.

691 The dependence on the undrained Poisson's ratio may be surprising, and it may
692 not be clear why having a pronounced undrained poroelastic response will result in a greater
693 stabilization. The analysis of Heimisson et al. (2021) provides some insight. The undrained
694 critical wavenumber is

$$|k_{cr}^{un}| \simeq \frac{2\sigma_0(b-a)(1-\nu_u)}{GL}\left(1 - \frac{f_0\gamma}{\beta\sigma_0(b-a)} + \mathcal{O}(\epsilon)\right), \tag{55}$$

695 and the corresponding drained wavenumber is

$$|k_{cr}^{d}| \simeq \frac{2\sigma_0(b-a)(1-\nu)}{GL}\left(1 - \frac{f_0\gamma}{\beta\sigma_0(b-a)} + \mathcal{O}(\epsilon)\right), \tag{56}$$

696 assuming the shear zone mobility tends to zero. Thus the ratio of the minimum unsta-
697 ble wavelength in drained and undrained limits is

$$\frac{\lambda_d}{\lambda_{un}} = \frac{1-\nu}{1-\nu_u}, \tag{57}$$

698 Thus, at most, this ratio can be 2, but more commonly around 1 – 1.5. In simple terms,
699 it means that a perturbation or a slip patch on the fault of length ΔL may be unstable
700 if the bulk responds in a drained manner. However, the patch or perturbation may need
701 to be up to $2\Delta L$ to be unstable if the bulk responds in an undrained manner. There are
702 a few things to note about this stabilization. First, that it depends on the bulk diffu-
703 sivity, length scale, and slip rate. The transition from a drained to undrained response
704 will depend on the characteristic bulk diffusion time $\sim 1/(ck^2)$ relative to how fast the
705 fault is slipping and the slip patch length scale (due to the k^2 dependence). Thus the
706 timing of stabilization by a transition from drained to undrained response is nontrivial.
707 Second, the drained and undrained limits are inadequate to characterize the stabiliza-
708 tion fully. Heimisson et al. (2021) showed that in an intermediate (neither drained nor
709 undrained) regime, the fault could be more stable than in the undrained regime. Finally,
710 since anti-plane sliding does not depend on Poisson's ratio, the same kind of stabiliza-
711 tion will not occur. This may lead to interesting directional effects in 3D simulations.

712 Panels **b** and **c** in Figures 3, 4, and 5 consistently show similar rupture propaga-
713 tion and stabilization. This suggests that, in a certain sense, that setting $\nu_u = 0.35$ is
714 approximately equally stabilizing as setting $c = 4 \cdot 10^{-7}$ m^2/s relative to the respec-
715 tive lower values in the simulation setup. Due to the many complexities mentioned in

the previous paragraph we don't think this will hold generally. However, simulations with combined $\nu_u = 0.35$ and $c = 4{\cdot}10^{-7}$ m^2/s are nearly identical regardless of the γ value (**a** in Figures 3, 4, and 5). This observation highlights that bulk effects through combined diffusion and poroelasticity can be so stabilizing that dilatancy never becomes significant enough to affect the rupture propagation and nucleation.

7 Conclusions

We have presented novel spectral boundary-integral (SBI) solutions applicable to frictional and fracture mechanics problems in a plane strain linear poroelastic solid. The solutions consider that the interface of two poroelastic half-spaces may undergo mode I and II displacement discontinuity as well as pressurization. We have applied the solutions to develop a method and code implementation of a rate-and-state fault that has simultaneous inelastic dilatancy and injection. We apply this code to data from a field experiment, which has been previously analyzed by modeling. We explore the role of inelastic dilatancy, bulk diffusion, and poroelastic properties of the bulk on the simulation results. We find, surprisingly, that bulk diffusion and poroelastic properties of the bulk, which are parameters that are rarely explored, can qualitatively affect rupture stability and propagation. Further, we find the stabilization of bulk diffusion and poroelastic properties can be comparable to the well-known stabilizing dilatancy mechanism.

Data Availability Statement

No original data is presented in this study. The data used in regard to application to the (Guglielmi et al., 2015) field experiment was archived by Larochelle et al. (2021b): CaltechDATA repository (`https://data.caltech.edu/records/1891`). The software implementation of the method described in this paper is available here `https://doi.org/10.5281/zenodo.6010353` (see Heimisson, 2022).

Acknowledgments

This study was supported by the Geophysics Option Postdoctoral Fellowship from the Division of Geological and Planetary Sciences at Caltech and ETH Postdoctoral fellowship (Project No. FEL-19 20-2) to E.R.H. The work was further supported by the NSF-IUCRC Center for Geomechanics and Mitigation of Geohazards (projects GMG-4.1, GMG-4.2) to N.L.

Appendix A Parameter values

Here we briefly explain how the parameter values, listed in the table below, are set.

Parameters G, ν, and all friction and loading parameters in Table A1 are from Larochelle et al. (2021a). Compressibilities $\beta_f^p, \beta_f^\sigma, \beta_n^p, \beta_n^\sigma, \beta_g^p, \beta_g^\sigma$ in addition to ϕ_0 and ϵ are selected as in Heimisson et al. (2021).

Skempton's coefficient is fixed and set to 0.85, this value is representative of Westerly granite as well as certain types of sandstone and other rocks. The undrained Poisson's ratio is, on one hand, set to 0.35 to reflect the approximate value of Westerly granite and on the other hand to 0.262 to represent the undrained value of Charcoal granite. We note that Charcoal granite has $\nu = 0.270$ and $\nu_u = 0.292$ (Cheng, 2016). However, we wish to fix ν such that we do have multiple parameters varying each simulation. Thus only the range $\nu_u - \nu$ is the same as for Charcoal granite albeit the Poisson's ratios are similar in absolute terms. Further, Charcoal granite has a substantially lower Skempton's coefficient $B = 0.454$, but we still use $B = 0.85$ again to limit the number of varying parameters. We, therefore, do not recommend using this paper as a reference for poroelastic parameters, but rather look at the overview of Detournay and Cheng (1995); Cheng (2016), which we used, and references therein for more information on error and methods for measuring. Here we simply want to explore two cases where $\nu_u - \nu$ small and large, but at the same time make sure that the ranges reflect real values measured in rocks.

As explained in the main text, the range of the dilatancy coefficient is selected to reflect three different styles of ruptures. First we set $\gamma = 0$ and $\gamma = 1.7 \cdot 10^{-4}$ as trial values where the latter is the standard value used and was identified by Segall and Rice (1995). We observed that the two values would typically render either highly unstable or very stable slip. Thus an value of $\gamma = 1.7 \cdot 10^{-5}$ was identified as producing sustained slow slip migration.

The two mobilities κ_{cx}, κ_{cy} and the bulk hydraulic diffusivity c were determined by trial and error by trying to approximately match the pore pressure evolution in Larochelle et al. (2021a). We highlight that due to the heterogeneous permeability structure, the fact that we treat the pore pressure as non-constant in the shear zone, and other cou-

pling mechanisms that alter the pore pressure, we cannot simply select parameters that give exactly the same pore pressure evolution as in Larochelle et al. (2021a).

Appendix B Method validation

The spectral boundary-integral method, in addition to the rate-and-state fault slip simulations, couples together several physical processes that could not be simulated with another individual code. Further, no analytical solutions are available that also couple all these processes. It is, therefore, nearly impossible to benchmark and test all capabilities of the code and implementation simultaneously. However, here we list to provide an overview of the tests and validation we carried out.

- As was reported in Figure 2 the SBI solutions for τ' and $p^{\pm}$ were tested against the solutions of (Song & Rudnicki, 2017).
- The analytical inversion of the Laplace transform was in all cases tested by also numerically inverting the Laplace transform numerically using the Talbot method (Talbot, 1979)
- Using p^{+} as the relevant pore pressure when computing the effective normal stress, we reproduced the results of (Heimisson et al., 2019), which were done with a different code (Torberntsson et al., 2018). We, for example, reproduced the spontaneously occurring instabilities at mildly rate-strengthening friction that give rise to slow-slip pulses, which only occur in a limited parameter regime. Our results were consistent with the spatial dimension of the instabilities and the pulse propagation speeds as reported by (Heimisson et al., 2019).
- Using the linearized stability analysis of (Heimisson et al., 2021) we identified the critical wavenumber for many different regimes, such as high diffusivity, low diffusivity, intermediate diffusivity as well as thicker and thinner shear zones. In the code, a fully non-linear implementation, we induced a critical wavelength perturbation, as determined by the linearized analysis, by introducing a small perturbation in the initial state around steady-state sliding. We found in all cases that the perturbation in the slip speed oscillated without growing or decaying.

The tests and benchmarking above do validate most aspects of the implementation and method we have introduced in this paper. However, none test the injection into the fault and fluid propagation as a result of the injection. In order to check the robust-

Table A1. Parameter values in the study

Symbol	Description	Value
Bulk and gouge material properties		
G	Shear modulus	10 GPa
B	Skempton's coefficient	0.85
ν	Drained Poisson's ratio	0.24
ν_u	Undrained Poisson's ratio	0.35, 0.262
β_f^p,β_f^σ	Isotropic and uniaxial fluid compressibility	$0.44 \cdot 10^{-9}$ Pa^{-1}, $0.24 \cdot 10^{-9}$ Pa^{-1},
β_n^p,β_n^σ	Isotropic and uniaxial pore volume compressibility	$6.0 \cdot 10^{-9}$ Pa^{-1}, $3.3 \cdot 10^{-9}$ Pa^{-1},
β_g^p,β_g^σ	Isotropic and uniaxial solid gouge compressibility	$0.020 \cdot 10^{-9}$ Pa^{-1}, $0.011 \cdot 10^{-9}$ Pa^{-1},
ϕ_0	Reference porosity	0.068
γ	Diltancy coefficient (Segall & Rice, 1995)	0, $1.7{\cdot}10^{-5}$, $1.7{\cdot}10^{-4}$
ϵ	Shear-zone half thickness	1.0 mm
c	Bulk hydraulic diffusivity	$4{\cdot}10^{-8}$, $4{\cdot}10^{-7}$ m^2/s
κ_{cx}	Along shear-zone mobility	$8.7584{\cdot}10^{-11}$ m^2/(Pa s)
κ_{cy}	Across shear-zone mobility	$8.7584{\cdot}10^{-20}$ m^2/(Pa s)
Friction and loading parameters		
L	Characteristic state evolution distance	16.75 μm
a	Direct rate dependence of friction	0.01125
b	State dependence of friction	0.016
α_{LD}	Linker and Dieterich (1992) constant	0.0
V_0	reference slip rate	10^{-6} m/s
f_0	reference friction	0.55
τ_0	Initial shear stress	2.15 MPa
σ_0	Initial effective normal stress	4 MPa

ness of the algorithm in this regard, we set up a problem with injection and delayed nucleation with dilatancy. The simulations are run until the slip speed reaches 1 cm/s, which we take as the instability time. This setup thus tests how well the pore pressure injection and subsequent diffusion is resolved as it promotes instability. We generate a manufactured solution with the error tolerance and state integration parameter set to $\xi = 1/4096$ (see section 4.2). Then setting $\xi \in \{1/4, 1/8, 1/16, 1/32, 1/64\}$ and investigating the L_1 norm error of the manufactured solution and the less accurate solutions plotted against the total number of iterations (which scales with the computational time) we see a second-order convergence. Where we look at the time of instability, the slip speed profile at the instability time, the p_c value at the instability time, and the slip profile at that time. $\xi = 1/32$ roughly correspond to a relative error of 10^{-3} in all the fields we looked at, but we stress that the magnitude of the relative error depends on the problem and the simulation time. For simulations we favor using $\xi = 1/32$ and one minimum iteration (see section 4.2 for discussion on iterations). If smaller values than $\xi = 1/64$ are compared to the manufactured solution, the convergence gets more complicated but tends to improve to the first order with the iteration number. Using no minimum iteration or 2 minimum iterations also works and gives consistent results. We suggest 1 minimum iteration is most efficient in terms of obtaining a stable convergent solution at the fewest total iterations.

Finally, we note that Figure 3c demonstrates, by chance, that the simulations are well resolved and accurate. A careful inspection of the figures shows that the last event is not one event but two events nucleating at exactly the same time around $x \approx \pm 30$ m and then coalescing. While such a high degree of symmetry is not physically realistic, it is a strong indication of well-resolved simulations in time and space, especially when it occurs not at the first simulated event. The same phenomenon also occurs in Figure 3b, but it is not as clear.

References

Ben-Zion, Y., & Rice, J. R. (1997). Dynamic simulations of slip on a smooth fault in an elastic solid. *Journal of Geophysical Research: Solid Earth*, *102*(B8), 17771-17784. doi: https://doi.org/10.1029/97JB01341

Bhattacharya, P., & Viesca, R. C. (2019). Fluid-induced aseismic fault slip outpaces pore-fluid migration. *Science*, *364*(6439), 464–468. doi: 10.1126/science.aaw7354

Bizzarri, A., & Cocco, M. (2006). A thermal pressurization model for the spontaneous dynamic rupture propagation on a three-dimensional fault: 1. Methodological approach. *Journal of Geophysical Research: Solid Earth*, *111*(B5). doi: https://doi.org/10.1029/2005JB003862

Bürgmann, R. (2018). The geophysics, geology and mechanics of slow fault slip. *Earth Planet. Sc. Lett.*, *495*, 112–134.

Cappa, F., Scuderi, M. M., Collettini, C., Guglielmi, Y., & Avouac, J.-P. (2019). Stabilization of fault slip by fluid injection in the laboratory and in situ. *Science Advances*, *5*(3), eaau4065. doi: 10.1126/sciadv.aau4065

Cheng, A. H.-D. (2016). *Poroelasticity* (Vol. 877). Springer.

Ciardo, F., & Lecampion, B. (2019). Effect of dilatancy on the transition from aseismic to seismic slip due to fluid injection in a fault. *Journal of Geophysical Research: Solid Earth*, *124*(4), 3724-3743. doi: https://doi.org/10.1029/2018JB016636

Dal Zilio, L., Lapusta, N., & Avouac, J.-P. (2020). Unraveling scaling properties of slow-slip events. *Geophysical Research Letters*, *47*(10). doi: 10.1029/2020GL087477

Detournay, E., & Cheng, A. H.-D. (1995). Fundamentals of poroelasticity. In *Analysis and design methods* (pp. 113–171). Elsevier.

Dieterich, J. H. (1979). Modeling of rock friction: 1. experimental results and constitutive equations. *Journal of Geophysical Research: Solid Earth*, *84*(B5), 2161-2168. doi: 10.1029/JB084iB05p02161

Duchon, C. E. (1979). Lanczos filtering in one and two dimensions. *Journal of applied meteorology*, *18*(8), 1016–1022.

Dunham, E. M., & Rice, J. R. (2008). Earthquake slip between dissimilar poroelastic materials. *J. Geophys. Res. Solid Earth*, *113*(B9). (B09304) doi: 10.1029/

2007JB005405

Ellsworth, W. L. (2013). Injection-induced earthquakes. *Science*, *341*(6142), 1225942.

Guglielmi, Y., Cappa, F., Avouac, J.-P., Henry, P., & Elsworth, D. (2015). Seismicity triggered by fluid injection–induced aseismic slip. *Science*, *348*(6240), 1224–1226. doi: 10.1126/science.aab0476

Hawthorne, J. C., & Rubin, A. M. (2013). Laterally propagating slow slip events in a rate and state friction model with a velocity-weakening to velocity-strengthening transition. *Journal of Geophysical Research: Solid Earth*, *118*(7), 3785-3808. doi: https://doi.org/10.1002/jgrb.50261

Heimisson, E. R. (2020). Crack to pulse transition and magnitude statistics during earthquake cycles on a self-similar rough fault. *Earth and Planetary Science Letters*, *537*, 116202. doi: https://doi.org/10.1016/j.epsl.2020.116202

Heimisson, E. R. (2022, February). *eliasrh/poro_sbim: Poro_sbim_v1.0.* Zenodo. Retrieved from `https://doi.org/10.5281/zenodo.6010353` doi: 10.5281/zenodo.6010353

Heimisson, E. R., Dunham, E. M., & Almquist, M. (2019). Poroelastic effects destabilize mildly rate-strengthening friction to generate stable slow slip pulses. *Journal of the Mechanics and Physics of Solids*, *130*, 262 – 279. doi: 10.1016/j.jmps.2019.06.007

Heimisson, E. R., Rudnicki, J., & Lapusta, N. (2021). Dilatancy and compaction of a rate-and-state fault in a poroelastic medium: Linearized stability analysis. *Journal of Geophysical Research: Solid Earth*, *126*(8), e2021JB022071. doi: https://doi.org/10.1029/2021JB022071

Hsieh, P. A., & Bredehoeft, J. D. (1981). A reservoir analysis of the denver earthquakes: A case of induced seismicity. *Journal of Geophysical Research: Solid Earth*, *86*(B2), 903-920. doi: https://doi.org/10.1029/JB086iB02p00903

Jha, B., & Juanes, R. (2014). Coupled multiphase flow and poromechanics: A computational model of pore pressure effects on fault slip and earthquake triggering. *Water Resources Research*, *50*(5), 3776-3808. doi: 10.1002/2013WR015175

Kaneko, Y., Ampuero, J.-P., & Lapusta, N. (2011). Spectral-element simulations of long-term fault slip: Effect of low-rigidity layers on earthquake-cycle

dynamics. *Journal of Geophysical Research: Solid Earth*, *116*(B10). doi: https://doi.org/10.1029/2011JB008395

Lapusta, N., Rice, J. R., Ben-Zion, Y., & Zheng, G. (2000). Elastodynamic analysis for slow tectonic loading with spontaneous rupture episodes on faults with rate- and state-dependent friction. *Journal of Geophysical Research: Solid Earth*, *105*(B10), 23765-23789. doi: https://doi.org/10.1029/2000JB900250

Larochelle, S., Lapusta, N., Ampuero, J.-P., & Cappa, F. (2021a). Constraining fault friction and stability with fluid-injection field experiments. *Geophysical Research Letters*, *48*(10), e2020GL091188. doi: https://doi.org/10.1029/2020GL091188

Larochelle, S., Lapusta, N., Ampuero, J.-P., & Cappa, F. (2021b). *Constraining fault friction and stability with fluid-injection field experiments.* CaltechDATA. Retrieved from `https://data.caltech.edu/records/1891` doi: 10.22002/D1.1891

Leeman, J., Saffer, D., Scuderi, M., & Marone, C. (2016). Laboratory observations of slow earthquakes and the spectrum of tectonic fault slip modes. *Nature communications*, *7*(1), 1–6. doi: https://doi.org/10.1038/ncomms11104

Linker, M. F., & Dieterich, J. H. (1992). Effects of variable normal stress on rock friction: Observations and constitutive equations. *J. Geophys. Res. Solid Earth*, *97*(B4), 4923–4940. doi: 10.1029/92JB00017

Liu, Y., & Rice, J. R. (2005). Aseismic slip transients emerge spontaneously in three-dimensional rate and state modeling of subduction earthquake sequences. *Journal of Geophysical Research: Solid Earth*, *110*(B8). doi: https://doi.org/10.1029/2004JB003424

Liu, Y., & Rice, J. R. (2007). Spontaneous and triggered aseismic deformation transients in a subduction fault model. *Journal of Geophysical Research: Solid Earth*, *112*(B9). doi: https://doi.org/10.1029/2007JB004930

Marone, C. (1998). Laboratory-derived friction laws and their application to seismic faulting. *Annu. Rev. Earth Pl. Sc.*, *26*(1), 643–696.

Marone, C., Raleigh, C. B., & Scholz, C. H. (1990). Frictional behavior and constitutive modeling of simulated fault gouge. *Journal of Geophysical Research: Solid Earth*, *95*(B5), 7007-7025. doi: 10.1029/JB095iB05p07007

McNamee, J., & Gibson, R. E. (1960). Plane strain and axially symmetric problems

of the consolidation of a semi-infinite clay stratum. *Q. J. Mech. Appl. Math.*, *13*(2), 210–227.

Noda, H., & Lapusta, N. (2013). Stable creeping fault segments can become destructive as a result of dynamic weakening. *Nature*, *493*(7433), 518–521. doi: https://doi.org/10.1038/nature11703

Proctor, B., Lockner, D. A., Kilgore, B. D., Mitchell, T. M., & Beeler, N. M. (2020). Direct evidence for fluid pressure, dilatancy, and compaction affecting slip in isolated faults. *Geophysical Research Letters*, *47*(16), e2019GL086767. doi: 10.1029/2019GL086767

Raleigh, C., Healy, J., & Bredehoeft, J. (1976). An experiment in earthquake control at rangely, colorado. *Science*, *191*(4233), 1230–1237. doi: 10.1126/science.191.4233.1230

Rice, J. R. (2006). Heating and weakening of faults during earthquake slip. *Journal of Geophysical Research: Solid Earth*, *111*(B5). doi: 10.1029/2005JB004006

Rice, J. R., & Ben-Zion, Y. (1996). Slip complexity in earthquake fault models. *Proceedings of the National Academy of Sciences*, *93*(9), 3811–3818. doi: 10.1073/pnas.93.9.3811

Rice, J. R., & Cleary, M. P. (1976). Some basic stress diffusion solutions for fluid-saturated elastic porous media with compressible constituents. *Rev. Geophys.*, *14*(2), 227–241. doi: 10.1029/RG014i002p00227

Rudnicki, J. W., & Chen, C.-H. (1988). Stabilization of rapid frictional slip on a weakening fault by dilatant hardening. *Journal of Geophysical Research: Solid Earth*, *93*(B5), 4745–4757. doi: 10.1029/JB093iB05p04745

Rudnicki, J. W., & Koutsibelas, D. A. (1991). Steady propagation of plane strain shear cracks on an impermeable plane in an elastic diffusive solid. *Int. J. Solids Struct.*, *27*(2), 205–225.

Rudnicki, J. W., & Rice, J. R. (2006). Effective normal stress alteration due to pore pressure changes induced by dynamic slip propagation on a plane between dissimilar materials. *J. Geophys. Res. Solid Earth*, *111*(B10). doi: 10.1029/2006JB004396

Ruina, A. (1983). Slip instability and state variable friction laws. *Journal of Geophysical Research: Solid Earth*, *88*(B12), 10359-10370. doi: 10.1029/JB088iB12p10359

Segall, P. (2010). *Earthquake and volcano deformation*. Princeton University Press.

Segall, P., & Lu, S. (2015). Injection-induced seismicity: Poroelastic and earthquake nucleation effects. *J. Geophys. Res. Solid Earth*, *120*(7), 5082–5103.

Segall, P., & Rice, J. R. (1995). Dilatancy, compaction, and slip instability of a fluid-infiltrated fault. *Journal of Geophysical Research: Solid Earth*, *100*(B11), 22155–22171. doi: 10.1029/95JB02403

Segall, P., & Rice, J. R. (2006). Does shear heating of pore fluid contribute to earthquake nucleation? *Journal of Geophysical Research: Solid Earth*, *111*(B9). doi: https://doi.org/10.1029/2005JB004129

Segall, P., Rubin, A. M., Bradley, A. M., & Rice, J. R. (2010). Dilatant strengthening as a mechanism for slow slip events. *J. Geophys. Res. Solid Earth*, *115*(B12).

Shibazaki, B., & Shimamoto, T. (2007, 10). Modelling of short-interval silent slip events in deeper subduction interfaces considering the frictional properties at the unstable—stable transition regime. *Geophysical Journal International*, *171*(1), 191-205. doi: 10.1111/j.1365-246X.2007.03434.x

Song, Y., & Rudnicki, J. W. (2017). Plane-strain shear dislocation on a leaky plane in a poroelastic solid. *J. Appl. Mech.*, *84*(2), 021008.

Talbot, A. (1979, 01). The Accurate Numerical Inversion of Laplace Transforms. *IMA Journal of Applied Mathematics*, *23*(1), 97-120. doi: 10.1093/imamat/23.1.97

Tong, X., & Lavier, L. L. (2018). Simulation of slip transients and earthquakes in finite thickness shear zones with a plastic formulation. *Nature communications*, *9*(1), 1–8. doi: https://doi.org/10.1038/s41467-018-06390-z

Torberntsson, K., Stiernström, V., Mattsson, K., & Dunham, E. M. (2018, Jul 19). A finite difference method for earthquake sequences in poroelastic solids. *Comput. Geosci.*, *22*(5), 1351–1370. doi: 10.1007/s10596-018-9757-1

Verruijt, A. (1971). Displacement functions in the theory of consolidation or in thermoelasticity. *Zeitschrift für angewandte Mathematik und Physik ZAMP*, *22*(5), 891–898.

Viesca, R. C., & Dublanchet, P. (2019). The slow slip of viscous faults. *Journal of Geophysical Research: Solid Earth*, *124*(5), 4959-4983. doi: https://doi.org/10.1029/2018JB016294

Wibberley, C. A., & Shimamoto, T. (2003). Internal structure and permeability of major strike-slip fault zones: the Median Tectonic Line in Mie Prefecture, Southwest Japan. *J. Struct. Geol.*, *25*(1), 59–78.

Yang, Y., & Dunham, E. M. (2021). Effect of porosity and permeability evolution on injection-induced aseismic slip. *Journal of Geophysical Research: Solid Earth*, *126*(7), e2020JB021258. doi: https://doi.org/10.1029/2020JB021258

Yehya, A., Yang, Z., & Rice, J. R. (2018). Effect of fault architecture and permeability evolution on response to fluid injection. *Journal of Geophysical Research: Solid Earth*, *123*(11), 9982-9997. doi: https://doi.org/10.1029/2018JB016550

Zhang, S., Tullis, T. E., & Scruggs, V. J. (1999). Permeability anisotropy and pressure dependency of permeability in experimentally sheared gouge materials. *Journal of Structural Geology*, *21*(7), 795-806. doi: https://doi.org/10.1016/S0191-8141(99)00080-2